Evolution of the Tropical Response to Periodic Extratropical Thermal Forcing

YECHUL SHIN,[a] SARAH M. KANG,[a] KEN TAKAHASHI,[b] MALTE F. STUECKER,[c] YEN-TING HWANG,[d] AND DOYEON KIM[a]

[a] *School of Urban and Environmental Engineering, Ulsan National Institute of Science and Technology, Ulsan, South Korea*
[b] *Servicio Nacional de Meteorología e Hidrología del Perú (SENAMHI), Lima, Peru*
[c] *Department of Oceanography and International Pacific Research Center, School of Ocean and Earth Science and Technology, University of Hawai'i at Mānoa, Honolulu, Hawaii*
[d] *Department of Atmospheric Sciences, National Taiwan University, Taipei, Taiwan*

(Manuscript received 30 June 2020, in final form 25 April 2021)

ABSTRACT: This study examines the temporal evolution of the extratropically forced tropical response in an idealized aquaplanet model under equinox condition. We apply a surface thermal forcing in the northern extratropics that oscillates periodically in time. It is shown that tropical precipitation is unaltered by sufficiently high-frequency extratropical forcing. This sensitivity to the extratropical forcing periodicity arises from the critical time required for sea surface temperature (SST) adjustment. Low-frequency extratropical forcing grants sufficient time for atmospheric transient eddies to diffuse moist static energy to perturb the midlatitude SSTs outside the forcing region, as demonstrated by a one-dimensional energy balance model with a fixed diffusivity. As the transient eddies weaken in the subtropics, a further equatorward advection is accomplished by the Hadley circulation. The essential role of Hadley cell advection in connecting the subtropical signal to the equatorial region is supported by an idealized thermodynamical-advective model. Associated with the SST changes in the tropics is a meridional shift of the intertropical convergence zone. Since the time needed for SST adjustment increases with increasing mixed layer depth, the critical forcing period at which the extratropical forcing can affect the tropics scales linearly with the mixed layer depth. Our results highlight the important role of decadal-and-longer extratropical climate variability in shaping the tropical climate system. We also raise the possibility that the transient behavior of a tropical response forced by extratropical variability may be strongly dependent on cloud radiative effects.

KEYWORDS: Energy transport; Hadley circulation; Teleconnections

1. Introduction

It is well known that tropical climate variability impacts the extratropical climate via atmospheric Rossby waves. For example, impacts of El Niño–Southern Oscillation (ENSO) reach the extratropical regions through atmospheric teleconnections, demonstrated by both observational datasets and model experiments (e.g., Bjerknes 1969; Horel and Wallace 1981; Hoskins and Karoly 1981; Sardeshmukh and Hoskins 1988; Trenberth et al. 1998; Alexander et al. 2002; Timmermann et al. 2018). The converse was recognized in Kraus (1977) that related subtropical droughts to extratropical temperature changes. However, the impact of extratropical climate variability on the tropical climate had not been widely appreciated until the mid-2000s, potentially because of the existence of a critical latitude in the subtropics that generally absorbs Rossby waves (e.g., Wallace and Gutzler 1981; Schneider and Watterson 1984; Hoskins and Ambrizzi 1993). Consequently, the dynamics of the intertropical convergence zone (ITCZ), a zonal band of heavy precipitation near the equator, had been commonly thought to be controlled by local processes (Xie 2004) until paleoclimate records pointed to the possibility of extratropical impacts on the tropics.

A number of paleoclimate records suggest a link between Northern Hemisphere (NH) high-latitude climate change and the ITCZ variability. Hydrological paleo-proxy reconstructions

from the eastern tropical Pacific (Koutavas and Lynch-Stieglitz 2004) and the western tropical Atlantic (Lea et al. 2003) indicate that the ITCZ over both the Pacific and Atlantic basins was displaced southward during the Last Glacial Maximum. The hydrological cycle of the tropical Atlantic underwent rapid and dramatic changes during warm interstadial and cold stadial times of the last glacial period (Peterson et al. 2000). Oxygen isotope records near Nanjing, China, suggest that East Asian monsoon intensity changed synchronously with Greenland temperatures on millennial time scales (Wang et al. 2001). Wet periods in northeastern Brazil were found during cold periods in Greenland, consistent with a southward ITCZ shift (Wang et al. 2004). The covariance of paleoclimate records from two remote locations in the NH high latitudes and the tropical regions motivated climate modeling studies to investigate the mechanism for extratropics-to-tropics teleconnection. For example, Chiang and Bitz (2005) performed model experiments by abruptly imposing additional sea ice cover that corresponds to the Last Glacial Maximum. The resultant NH-wide cooling was shown to be associated with a southward ITCZ shift. More modeling studies followed that aimed at revealing the ability of extratropical thermal perturbations in shifting the ITCZ position. A sustained addition of freshwater to the subpolar North Atlantic in a model causes a slowdown of the Atlantic meridional overturning circulation (AMOC), resulting in a colder North Atlantic and a southward ITCZ shift (Zhang and Delworth 2005; Broccoli et al. 2006; Stouffer et al. 2006). Large-scale afforestation in the NH midlatitude warms the region by absorbing

more solar energy, leading to a northward ITCZ shift (Swann et al. 2012; Kang et al. 2015a). In the other hemisphere, a Southern Ocean cooling induced by Antarctic meltwater shifts the ITCZ to the north (Bronselaer et al. 2018). The equilibrium climate response to different radiative forcing agents such as black carbon and sulfate indicates that the ITCZ shifts toward the hemisphere with more positive (or less negative) radiative forcing in the annual mean (Yoshimori and Broccoli 2008).

Kang et al. (2008, 2009) investigated the mechanism for the extratropics-originated teleconnections by examining how the atmospheric energy budget and the associated zonal-mean ITCZ responds to the interhemispheric asymmetry of net energy flux into the atmosphere. As an imbalance between the hemispheric energy budget is introduced, the Hadley circulation adjusts to transport the energy surplus toward the cooler hemisphere via its upper branch, thus resulting in increased low-level moisture transport and a corresponding ITCZ shift into the warmer hemisphere. This energetic framework suggests that the magnitude of a meridional ITCZ shift is proportional to the cross-equatorial atmospheric energy transport (Broccoli et al. 2006; Kang et al. 2008), with the proportionality determined by the net energy input to the tropical atmospheric column (Bischoff and Schneider 2014). The framework has limitations as it discounts changes in gross moist stability (Seo et al. 2017; Wei and Bordoni 2018; Hill 2019), variations in the vertical profile of tropical ascent (Biasutti and Voigt 2020), transient eddies (Xiang et al. 2018), ocean dynamics (Kay et al. 2016; Hawcroft et al. 2017), and regional (nonzonal mean) features (Roberts et al. 2017). Nevertheless, the framework has provided significant insight into variations in the zonal-mean ITCZ location (Donohoe and Voigt 2017; Kang et al. 2018a; Kang 2020). For example, the energetic framework provides a simple explanation for how the ITCZ responds to a wide variety of perturbations ranging from paleoclimatic forcing (Donohoe et al. 2013) to orbital insolation variations (Bischoff et al. 2017) to global warming (Frierson and Hwang 2012) to remote extratropical forcing agents (Kang 2020) as well as for the fundamental question as to why the mean ITCZ is located in the NH (Frierson et al. 2013; Donohoe et al. 2013; Marshall et al. 2014; Kang et al. 2015b).

While most modeling studies examine the equilibrium tropical response to a time-invariant extratropical forcing, which is nicely explained by the energetic framework, some studies have evaluated the transient features of extratropics-to-tropics teleconnection. An abrupt addition of the NH high-latitude sea ice cover is shown to induce a pronounced southward ITCZ shift after 12–15 months in an atmospheric model coupled with a 50-m mixed layer slab ocean (Chiang and Bitz 2005; Mahajan et al. 2011). When coupled with a 2.4-m mixed layer slab ocean, an extratropical thermal forcing perturbs the equatorial region within 2–4 months (Kang et al. 2014). The response time scale of the ITCZ shift to an extratropical thermal forcing has been extensively examined in an aquaplanet global climate model coupled to a slab ocean (Woelfle et al. 2015). It was found that the time scale is linearly proportional to the mixed layer depth: from 1.6 months for a 2.4-m mixed layer to 16.8 months for a 50-m mixed layer. This linearity implies an importance of the SST response in the extratropics-to-tropics

teleconnection, consistent with previous studies showing that the extratropical impact on the ITCZ is mediated by SST changes (Cvijanovic and Chiang 2013; Singh et al. 2017; Voigt et al. 2017).

Despite the flurry of evidence of extratropics-to-tropics teleconnection from paleoclimate proxies and model experiments, we still lack observational evidence from modern records, particularly on time scales shorter than decadal. In one of few observational studies, Green et al. (2017) found a connection between extratropical SST variability and variations in the ITCZ position on multidecadal time scales but not on interannual time scales. In fact, one might think that the extratropics-to-tropics teleconnection on short (i.e., seasonal and interannual) time scales has been already demonstrated by Donohoe et al. (2013, 2014), who showed a robust relationship between the ITCZ position and the hemispheric contrast in net energy input (NEI) across a wide range of time scales in both observations and climate models. However, this robust relationship does not necessarily indicate the extratropically forced teleconnection unless the interhemispheric NEI contrast largely originates from the extratropics.

One obvious reason for limited observational evidence at decadal-and-shorter time scales is a large internal variability, but we believe there to be more physical grounds. It may be difficult to take an observational approach to identify the extratropics-to-tropics teleconnection partly due to the compensating effect from ocean dynamics. When the atmosphere is coupled with a dynamic ocean rather than a slab ocean, extratropical radiative perturbations become less efficient at inducing changes in the tropical rainfall because ocean dynamics reduce the load of the atmospheric energy transport (Deser et al. 2015; Kay et al. 2016). The extratropical impact on the tropics may have been overemphasized considering that earlier modeling studies assumed a passive ocean. How ocean dynamics modulates the extratropics-to-tropics teleconnection is an active area of current research (e.g., Green and Marshall 2017; Schneider 2017; Hawcroft et al. 2017; Kang et al. 2018a,b; White et al. 2018; Green et al. 2019; Yu and Pritchard 2019; Stuecker et al. 2020; Kang 2020) and is the focus of the Extratropical–Tropical Model Intercomparison Project (Kang et al. 2019, 2020).

Another reason would be associated with the time scale of extratropics-to-tropics teleconnection. The time scale for steady extratropical forcing to induce a prominent ITCZ shift is reported to be about 1.5 years in an atmospheric model coupled with a 50-m mixed layer slab ocean (Chiang and Bitz 2005; Mahajan et al. 2011; Woelfle et al. 2015). However, extratropical climate variability in the real world occurs at a wide range of time scales from annual (e.g., sea ice melt) to multidecadal (e.g., AMOC modulation). The time scale for transient extratropical forcings to affect the tropics might be longer than that for steady forcings. For instance, a Q flux–forced Atlantic multidecadal variability (AMV) in a climate model induces an ITCZ shift with a 4-yr lag while the (unforced) internally generated AMV induces an ITCZ shift with a 24-yr lag (Moreno-Chamarro et al. 2020). Furthermore, open-ocean convection in the Weddell Sea that occurs approximately every 75 years in a climate model simulation induces a cross-equatorial atmospheric energy transport response with a 12-yr

lag (Cabré et al. 2017). Thus, the long time scale for transient extratropical climate variability to perturb the tropics could hamper the observational identification of extratropics-to-tropics teleconnection. The question then naturally arises as to what determines the time scale for extratropics-to-tropics teleconnection. In this study, we explore the temporal evolution of the tropical climate response to periodically time-varying extratropical forcing at various frequencies. Despite the importance of ocean dynamics, it is often difficult to understand the coupled mechanism due to disentangled processes of each component in the system. We hence employ a passive ocean model, which allows us to focus on the fundamental atmospheric dynamics.

The manuscript is organized as follows. In section 2, we outline the model description and experimental configurations. In section 3, we invoke the energetic framework to understand the transient evolution, which suggests an important role of SST anomaly propagation for the extratropics-to-tropics teleconnection. We further examine the sequential mechanism by which an extratropical thermal forcing perturbs the tropics in section 4. An energy balance model suggests that diffusive eddies are in charge of an equatorward SST propagation in the midlatitudes. As the eddy activities weaken in the subtropics, the Hadley circulation takes over to advect moist static energy into the deep tropics, as demonstrated by an idealized thermodynamical-advective model. Then we additionally explore the role of cloud radiative effects in modulating the extratropically forced teleconnection pattern in section 5. We finally offer conclusions in section 6.

2. Model and experimental configuration

The model employed in this study is an atmospheric general circulation model AM2.0 developed at the Geophysical Fluid Dynamics Laboratory (GFDL) (Anderson et al. 2004), which participated in both phases 3 and 5 of the Coupled Model Intercomparison Project (CMIP3 and CMIP5). The model resolution is 2° latitude × 2.5° longitude with 24 vertical levels. The model is run under a perpetual equinox condition; that is, the seasonal variation is absent. AM2.0 is coupled to an aquaplanet slab ocean so that the SST (denoted as T_s) is interactively computed based on the surface energy budget:

$$C_o \frac{\partial T_s}{\partial t} = \text{SFC} + Q. \tag{1}$$

The specified heat capacity of oceanic mixed layer C_o is a product of seawater density, seawater specific heat, and the mixed layer depth. For a set of standard experiments, we specify C_o as 2×10^8 J K^{-1} m^{-2}, approximately corresponding to a 50-m mixed layer depth h_o. We examine the sensitivity to the ocean heat capacity in section 3. SFC is the net downward surface energy flux, and Q is the imposed surface heat flux forcing. Note that the SSTs are allowed to drop below the freezing temperature without forming any sea ice.

The form of imposed surface heat flux (called "Q flux") is zonally symmetric with a periodically oscillating amplitude in time:

$$Q(t, \varphi) = \frac{h_o A}{T} \sin\left(\frac{2\pi}{T}t\right) H(\varphi - \varphi_0). \tag{2}$$

Here, $H(x)$ is the Heaviside function, with $H(x) = 1$ for $x \geq 0$ and $H(x) = 0$ for $x < 0$, and the equatorward edge of the Q flux forcing $\varphi_0 = 40°$N. Hence, poleward of $\varphi_0 = 40°$N, the Q flux amplitude is a sinusoidal function of time, with a period T and a maximum amplitude $h_o A/T$. For a standard set of experiments with $h_o = 50$ m, we set the parameter $A = 1$ W yr m^{-3} and alter T between 1, 3, 5, and 10 years. The perturbation experiments are labeled based on the specified forcing period. For example, E1 refers to the experiment with $T = 1$ year. The imposed Q flux forcing is displayed in Fig. 1a. We set the Q flux amplitude as a function of both T and h_o in Eq. (2) in order to constrain the amplitude of SST fluctuation to be independent of those two factors. Consequently, the SST anomalies over the forcing region fluctuate within a similar range regardless of T (Fig. 1b). However, precisely speaking, the local SST response slightly decreases with the forcing period as discussed in section 3. The reference experiment is run with no surface heat flux perturbation ($A = 0$), which is integrated for 120 years including a 30-yr spinup period.

We also conduct a modified experiment to investigate how the cloud radiative effects (CRE) modulate the equatorward propagation of the extratropical thermal forcing. In particular, the E10 experiment is repeated with the cloud properties (cloud water mixing ratio, cloud ice mixing ratio, and cloud fractional area) prescribed to an arbitrarily selected 1-yr time series from the reference experiment at every 3 h in the radiative scheme (e.g., Kim et al. 2018). The E10 experiment with the suppressed CRE is labeled E10_CEF (for "cloud effect fixed").

We integrate all perturbation experiments for 150 years. In AM2.0 aquaplanet simulations, the temperature response to prescribed surface cooling is larger than that to prescribed surface warming due to nonlinear cloud radiative effects (e.g., Seo et al. 2014; Shaw et al. 2015; Shin et al. 2017). As a result, even though the periodic Q flux neither adds nor subtracts any energy from the global system in the time mean, the global mean SST slightly decreases by 0.4 K during the initial adjustment period for about 30 years (gray in Fig. 1b). Therefore, the first 30 years are discarded as a spinup period in all experiments. The composite of the climate response is computed as the average response for $n = 120, 40, 24$, and 12 cycles in E1, E3, E5, and E10, respectively. Table 1 summarizes all experiments.

3. The ITCZ response to periodic extratropical forcing

We first examine SST and precipitation response to the time-varying forcing. To isolate the Q flux–forced response, a Lanczos low-pass filter with one-quarter of T cutoff period is applied before calculating the composite across the respective forcing cycle. Figure 2 compares the SST and precipitation response composite for the experiments with a varying period. Although the magnitude of SST fluctuations is broadly similar in the extratropics (Figs. 1b and 2), the tropical precipitation response exhibits a strong sensitivity to the forcing period T.
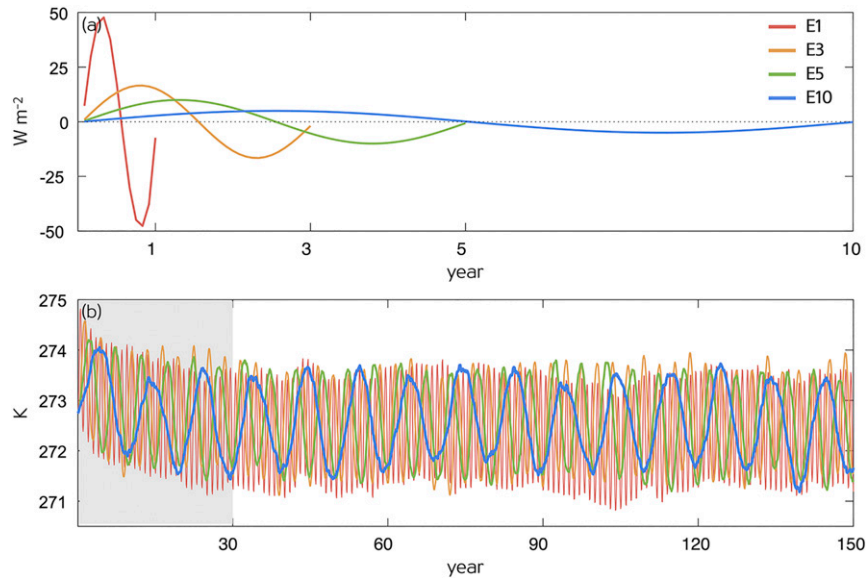
FIG. 1. Time series of (a) the imposed Q flux and (b) the SST averaged over the forcing region (poleward of 40°N) for the E1 (red), E3 (orange), E5 (green), and E10 (blue) experiments. Gray shading indicates the initial adjustment period.

The E3, E5, and E10 experiments show the SST response with an equatorward propagation and the tropical precipitation response with a clear periodicity, whereas the E1 experiment shows the SST response confined to the extratropics and a muted tropical precipitation response. In our model configuration, the extratropics-to-tropics teleconnection is evident only when the extratropical forcing period is equal to or longer than 3 years (Fig. 2). This implies that high-frequency variabilities in

TABLE 1. Overview of all experiments. The amplitude parameter A determines the total amount of anomalous energy imposed in the slab ocean during half of forcing period T.

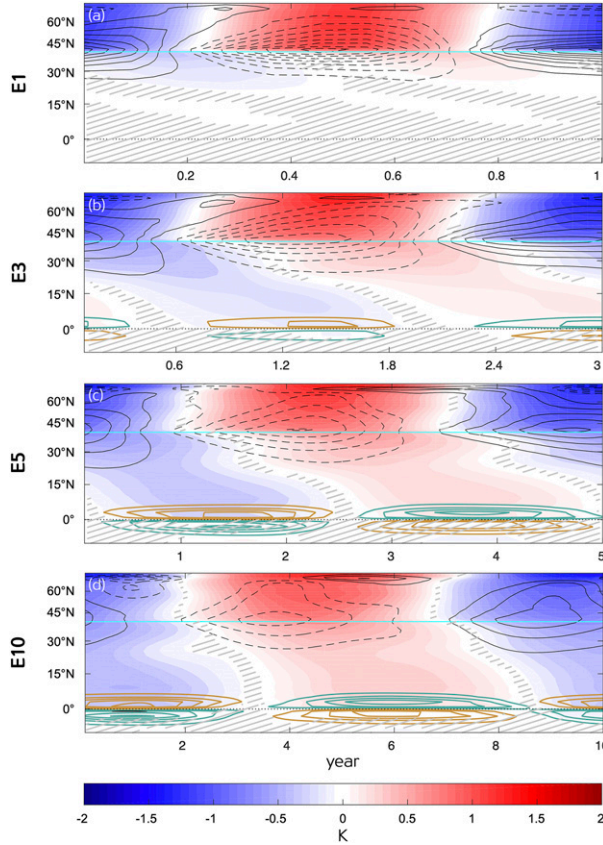| Experiment	Parameter A (W yr m^{-3})	Period T (yr)	Mixed layer depth h_o (m)	Feedback
E1	1	1	50	Interactive
E3		3		
E5		5		
E10		10		
E6mo_40m		1/2	40	
E1_40m		1		
E3_40m		3		
E6mo_30m		1/2	30	
E1_30m		1		
E3_30m		3		
E6mo_20m		1/2	20	
E1_20m		1		
E3_20m		3		
E1_10m_5A	5	1	10	
E1_10m_1p5A	1.5			
E1_10m_0p5A	0.5			
E1_10m	1			
E1mo_10m		1/12		
E1_5m		1	5	
E1mo_5m		1/12		
E1_2p5m		1	2.5	
E0p5mo_2p5m		1/24		
E10_WEF		10	50	WES suppressed
E10_CEF			25	CRE suppressed
E10_CEF_25m			10	
E10_CEF_10m				

FIG. 2. Composite across the forcing cycle of zonally averaged response of SST (shading; K), precipitation (green/brown contour; interval = 1 mm day^{-1}), and meridional eddy heat flux at 900 hPa (northward in black solid and southward in black dashed; interval = 0.3 K m s^{-1}) for the (a) E1, (b) E3, (c) E5, and (d) E10 experiments. The equatorial edge of the forcing region ($\varphi_0 = 40°$N) is indicated by a cyan line. Hatched regions denote statistically insignificant values at the 95% confidence level based on a two-sided Student's t test.

FIG. 3. The response time scale τ_{eq} as a function of mixed layer depth h_o in a model with interactive radiative feedbacks. The gray line indicates the lag time of maximum correlation coefficient between the SST anomaly at the Q flux edge and at the Hadley circulation terminus (τ_{HC}), averaged over all available experiments with the same h_o, with ± 1 standard deviation in shading. The critical forcing period T_{crit} can be estimated as $2 \times \tau_{HC}$. Colors demarcate the forcing period T as indicated in the legend. For the experiments with no extratropically forced teleconnection, a half of the forcing period T is indicated by cross symbols. For the experiments with the forcing amplitude different from A, the forcing amplitude is indicated by the text next to the symbols.

the extratropics, such as the seasonal variation of high-latitude ice cover, would hardly affect the tropical climate, whereas low-frequency variabilities in the extratropics, such as the Atlantic multidecadal variability, would be more likely to perturb the tropical climate. Figure 3 summarizes the response time scale τ_{eq}, calculated as the lag time at which the correlation coefficient is maximized between the SST anomaly at the Q flux edge ($\varphi_0 = 40°$N) and that at the equator. The response time scale τ_{eq} is 1.33, 1.52, and 1.58 years in E3, E5, and E10, respectively (green-blue circles for $h_o = 50$ m in Fig. 3), generally consistent with Woelfle et al. (2015; see their Fig. 3b). This time scale is much longer than that for teleconnections originating from the tropics, which amounts to approximately two weeks (e.g., Li et al. 2014). This long time scale would make it difficult to observe the atmospheric teleconnection originating from the extratropics.

Then, what causes the sensitivity to the extratropical forcing period? We seek to find the answer by diagnosing the atmospheric energy budget:
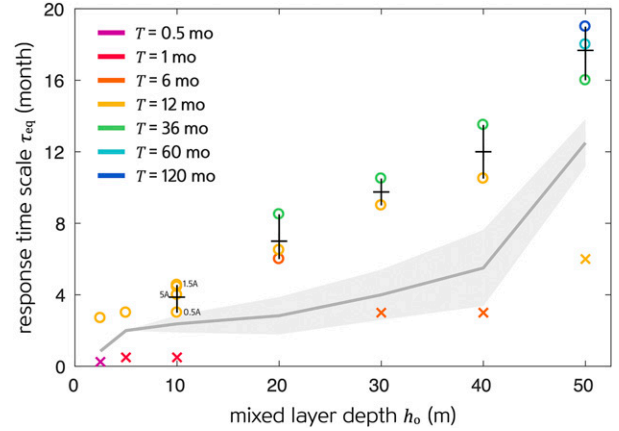
$$R_{\text{TOA}} - \text{SFC} = \frac{\partial}{\partial t}\langle c_p T + L_v q \rangle + \nabla \cdot F_A, \quad (3)$$

which states that the net energy input, the difference between the net downward top-of-atmosphere (TOA) radiation R_{TOA} and the net downward surface energy flux SFC, equals the sum of the time tendency of atmospheric column energy (with the angle brackets denoting the vertical integral, L_v the heat of vaporization, and c_p the specific heat of dry air) and the divergence of atmospheric energy transport F_A. We neglect the atmospheric column energy tendency as it is small compared to other components (not shown). To express Eq. (3) in a flux form, we subtract the global average, integrate around the latitude circle, and integrate over the latitude from the South Pole:

$$\nabla \cdot (F_A + F_R + F_S) = 0, \quad (4)$$

where

$$F_R(\phi) \equiv -a^2 \int_{-\pi/2}^{\phi} \int_0^{2\pi} (R_{\text{TOA}} - R_{\text{TOA}}^*) \cos\phi \, d\lambda \, d\phi, \quad (5)$$

$$F_S(\phi) \equiv a^2 \int_{-\pi/2}^{\phi} \int_0^{2\pi} (\text{SFC} - \text{SFC}^*) \cos\phi \, d\lambda \, d\phi, \quad (6)$$

with asterisks denoting the global average; Earth's radius is a, latitude ϕ, and longitude λ. We remove the global mean to ensure that the fluxes vanish at both poles. Note that the negative sign of R_{TOA} is used because a convergence of F_R corresponds to radiative heating and a divergence of F_R corresponds to radiative cooling. Figure 4 compares these energy
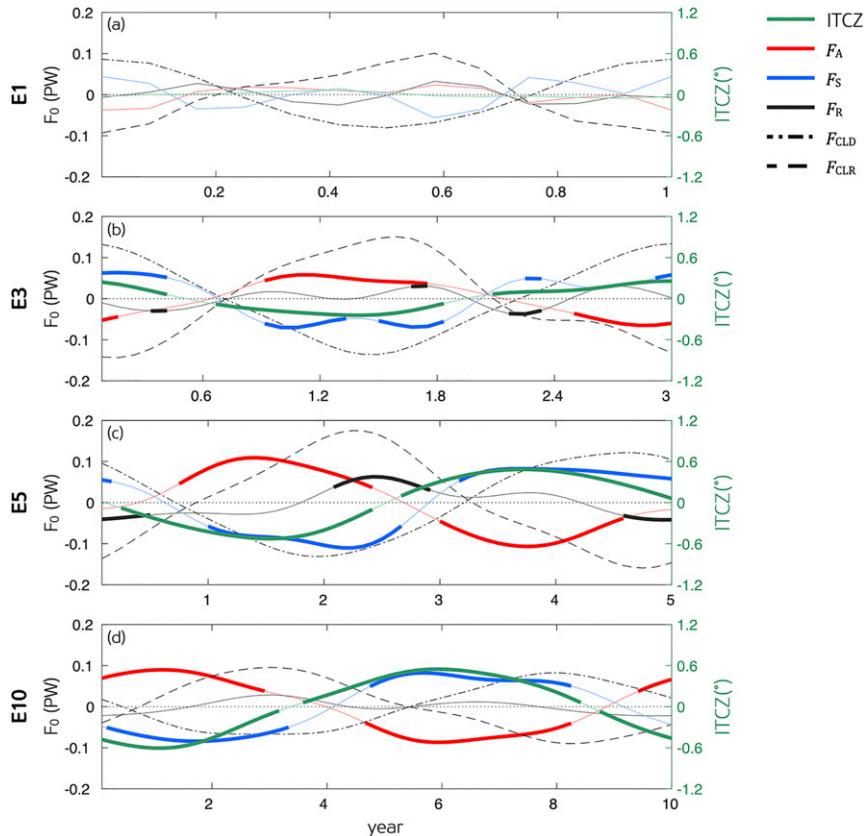
FIG. 4. Composite across the forcing cycle of the meridional ITCZ displacement (green; °
latitude) and the anomalous energy fluxes at the equator corresponding to change in TOA
radiation (black; for clear sky in dash-dotted and for cloudy sky in dashed), atmosphere (red),
and net surface flux (blue) for the (a) E1, (b) E3, (c) E5, and (d) E10 experiments. The terms are
defined in the legend and discussed in the text in reference to Eqs. (4)–(6). Thick line denotes
statistically significant values at the 95% confidence level relative to the internal variability
based on a two-sided Student's *t* test.

flux responses at the equator and the ITCZ location defined as
the latitude centroid of zonal-mean precipitation between 10°S
and 10°N. The ITCZ location in E1 is indistinguishable from
the internal variability estimated from the reference experi-
ment, while the ITCZ position in other experiments with $T \gtrsim 3$
years (E3, E5, and E10) undergoes a clear quasi-sinusoidal
temporal evolution. For $T \geq 3$ years (Figs. 4b–d), the ITCZ
location response (green) is completely out of phase with the
atmospheric energy flux response δF_A at the equator (red).
(The δ notation denotes the difference between the perturbed
and climatology.) This ensures the usefulness of the energetic
framework in understanding the temporal evolution of the
tropical precipitation response.

In all standard experiments (Fig. 4), the TOA radiation re-
sponse δF_R (black) is too small to make a discernible impact on
δF_A as a result of the cancellation between the cloud δF_{CLD}
(black dashed) and clear-sky δF_{CLR} (black dash-dotted) com-
ponents. Hence, the energetic framework indicates that the
equatorial δF_A, which is closely linked to the ITCZ response, is
balanced by the equatorial δF_S. The E3, E5, and E10 with a

clear ITCZ response exhibit a periodically oscillating surface
flux response δF_S at the equator (blue in Figs. 4b–d), whereas
the E1 with negligible ITCZ response exhibits a statistically
insignificant equatorial δF_S (Fig. 4a). The covariance between
δF_A and δF_S exists globally as displayed in the left and right
panels of Fig. 5, respectively. In all experiments, δF_S exhibits a
clear oscillatory evolution in the vicinity of φ_0 ($= 40°$N, cyan in
Fig. 5): however, the δF_S oscillation is confined to the forcing
region in E1 (Fig. 5b) while it propagates into the tropics in E3,
E5, and E10 (Figs. 5d,f,h). The F_S response outside the forcing
region corresponds to the ocean heat storage response for a
slab ocean, which is directly related to the SST tendency based
on Eq. (1). That is, the equatorward propagation pattern of δF_S
is a manifestation of the SST response. Although the magni-
tude of SST response is largely similar within the forcing region
(Fig. 1b), the SST response outside the forcing region shows a
stark dependency on the forcing period: the larger the forc-
ing period, the stronger the SST response outside the forcing
region (Fig. 2). In fact, lower-frequency forcing exhibits a
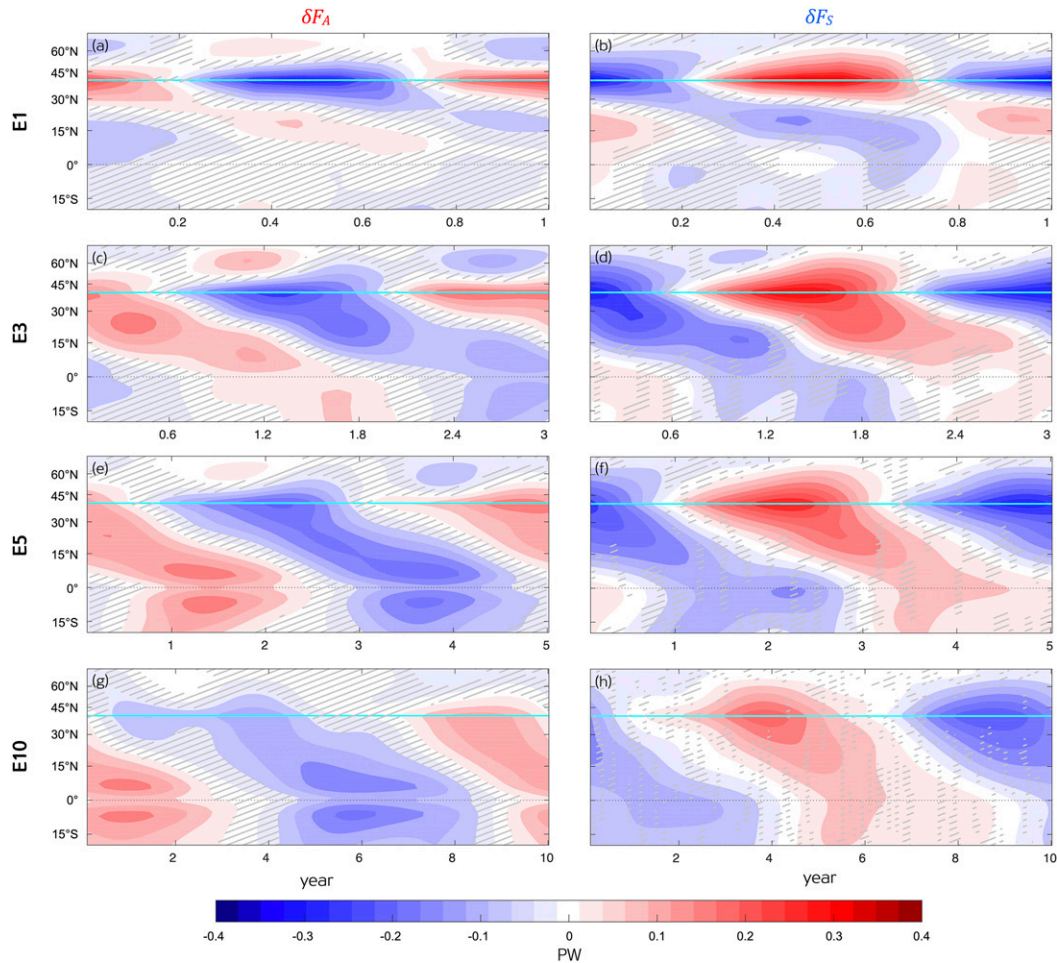slightly weaker local SST response, as noted in section 2, as a

FIG. 5. Composite across the forcing cycle of zonally averaged (left) δF_A and (right) δF_S for the (a),(b) E1, (c),(d) E3, (e),(f) E5, and (g),(h) E10 experiments (units are PW). The equatorial edge of the forcing region ($\varphi_0 = 40°N$) is indicated by a cyan line. Hatched regions denote statistically insignificant values at the 95% confidence level based on a two-sided Student's t test.

consequence of the extratropical signals spreading out to lower latitudes. The SST response is confined to the vicinity of φ_0 in E1 (Fig. 2a), consistent with little equatorward propagation of F_S response (Fig. 5b). In contrast, for $T \geq 3$ years, the SST response clearly propagates equatorward (Figs. 2b–d), and so does the F_S response (Figs. 5d,f,h). Our results suggest that extratropical energy perturbations can alter the tropical precipitation only when accompanied by an equatorward propagation of the SST response. Therefore, tropical precipitation can be expected to hardly respond if tropical SSTs are prescribed, a limiting case where the extratropical signal can be thought of as completely damped before it propagates into the tropics (Cvijanovic and Chiang 2013; Voigt et al. 2017).

The importance of an equatorward propagation of SST anomalies on the extratropics-to-tropics teleconnection is further demonstrated by additional experiments with shallower mixed layer depth h_o (i.e., smaller heat capacity of slab ocean C_o). We repeat the E1 experiment with a reduced C_o by a factor of 5, corresponding to the 10-m mixed layer (labeled

E1_10m). As the maximum amplitude [$h_o A/T$ from Eq. (2)] is also reduced by a factor of 5, the extratropical SST anomalies in E1_10m are of comparable magnitude to those in E1 (Figs. 2a and 6b). Nevertheless, the climate response equatorward of the forcing region is distinct between the two experiments. While the $T = 1$ yr forcing is ineffective at shifting the ITCZ in the standard setting with the 50-m mixed layer (Fig. 2a), reducing the mixed layer depth to 10 m enables the same forcing to induce a clear equatorward progression of SST anomalies and a periodic ITCZ shift (Fig. 6b). We further examine the sensitivity to the magnitude of extratropical SST anomalies by varying the parameter A from the E1_10m experiment: $A = 0.5$ in E1_10m_0p5A and $A = 5$ in E1_10m_5A. (Note that $A = 1$ in E1_10m.) As the extratropical SST response is amplified approximately by a factor of 5 in E1_10m_5A compared to E1_10m (contrast Figs. 6a and 6b), there certainly is an equatorward propagation of stronger SST anomalies and a larger meridional ITCZ shift but the response time scale τ_{eq} stays nearly the same (yellow circles for
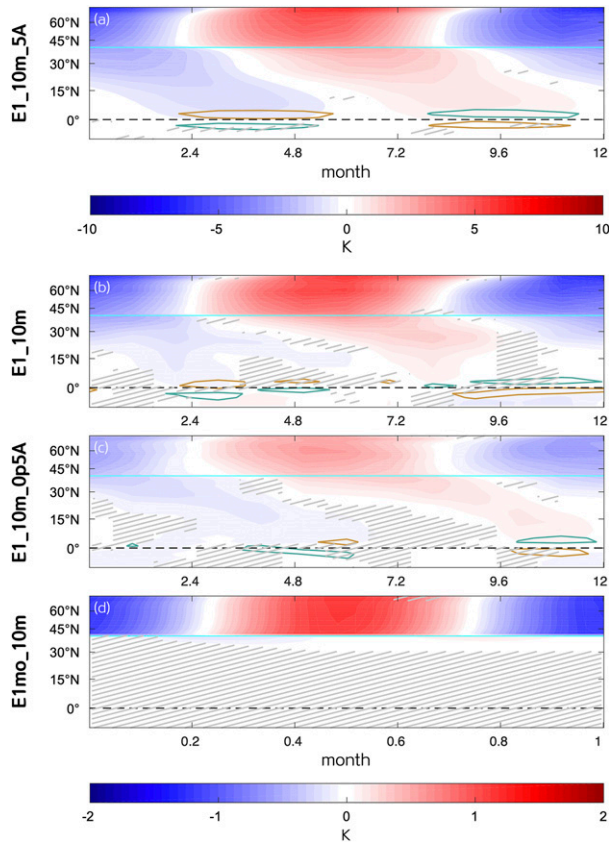
FIG. 6. Composite across the forcing cycle of zonally averaged response of SST (shading; K) and precipitation (green/brown contour; interval = 5 mm day^{-1} for E1_10m_5A and 1 mm day^{-1} for others) of (a) E1_10m_5A, (b) E1_10m, (c) E1_10m_0p5A, and (d) E1mo_10m. The equatorial edge of the forcing region ($\varphi_0 = 40°$N) is indicated by a cyan line. Hatched regions denote statistically insignificant values at the 95% confidence level based on a two-sided Student's t test.

$h_o = 10$ m in Fig. 3). Conversely, as the extratropical SST anomalies are halved in E1_10m_0p5A compared to E1 (contrast Figs. 6b and 6c), the tropical SST and precipitation responses become weaker but the teleconnection clearly emerges with a similar response time scale τ_{eq} (Fig. 3). Regardless of the forcing amplitude, the response time scale τ_{eq} in the 10-m mixed layer simulation is about 4 months (Figs. 6a–c), which amounts to one-fifth of τ_{eq} in the standard 50-m mixed layer simulations (Fig. 3). Additional experiments with a varying mixed layer depth indicate that $\tau_{eq} = 2.66, 2.67, 3.86, 6.83, 9.75, 12.1$, and 17.72 months for $h_o = 2.5, 5, 10, 20, 30, 40$, and 50 m, respectively. Consistent with Woelfle et al. (2015), the response time scale τ_{eq} scales linearly with the slab ocean heat capacity but is nearly invariant to the forcing amplitude. For a shallower mixed layer depth, the response time scale shortens, allowing for a higher-frequency extratropical forcing to extend the SST anomalies to the tropics and displace the ITCZ location. Thus, the extratropical forcing with $T = 1$ yr does not induce any tropical response for $h_o = 50$ m (yellow

cross) while the same forcing is able to perturb the tropics for $h_o \le 40$ m (yellow circles in Fig. 3).

4. Propagation mechanism

Previous sections indicate that a periodic extratropical forcing can induce a meridional ITCZ shift only with the SST propagation into the deep tropics. Next, we set out to understand the sequential processes of equatorward SST propagation. Although the energetic framework is proven useful for interpreting the ITCZ response to radiative perturbations, it is diagnostic rather than prognostic, providing little information about the propagation mechanism. Chiang and Bitz (2005) proposed the wind–evaporation–SST (WES) feedback as the dominant mechanism for the equatorward propagation of the high-latitude signal. However, suppressing the WES feedback had little impact on the tropical response to extratropical forcing in different climate models (Mahajan et al. 2011; Kang and Held 2012; Kang et al. 2014). Other studies hinted at the possible roles of transient eddies in the extratropics and the Hadley circulation in the tropics based on their relative importance in transporting the moist static energy at different latitudinal regimes (e.g., Broccoli et al. 2006; Kang et al. 2009). However, in an experiment where energy flux perturbations are abruptly introduced, it is often difficult to disentangle the sequential order of multiple dynamical processes at work without a large number of ensemble members. In contrast, our experiment setup with periodical forcing allows us to objectively differentiate the sequential order of different physical processes based on the phase lag between the extratropical forcing and the response of any variable of interest.

The SSTs outside the forcing region are only a function of net surface energy flux determined by the local air–sea interaction in a slab ocean model; thus, we first examine how the atmospheric moist static energy (MSE) propagates away from the forcing region. Figure 7a shows the lag time at which the correlation coefficient is maximized between the zonal-mean tropospheric MSE anomalies and the Q flux forcing in the standard experiment with $T = 10$ yr (E10). This time lag distribution in latitude and pressure illustrates the zonal-mean MSE propagation pattern as a smaller time lag indicates that the MSE response is established faster at a given location. The impact of extratropical forcing propagates upward and equatorward simultaneously. On the equatorward side of the forcing edge (40°N), the fastest propagation takes place near the surface, implying that the most preferential pathway for extratropical perturbations to reach the tropics is through the lower troposphere. This propagation pattern is largely shared by other experiments in which the extratropically forced teleconnection emerges (Fig. 8). The rapid lower tropospheric propagation can be further confirmed by a Hovmöller diagram of the zonal-mean MSE response at different vertical levels (Figs. 7b–d). The MSE response at 850 hPa propagates equatorward from the extratropical forcing region (Fig. 7d) whereas at higher levels the tropical response emerges earlier than the extratropical response, indicative of a poleward propagation (Figs. 7b,c). That is, the mid-to-upper tropospheric MSE in the subtropics responds only after the near-surface propagation reaches the deep tropics.
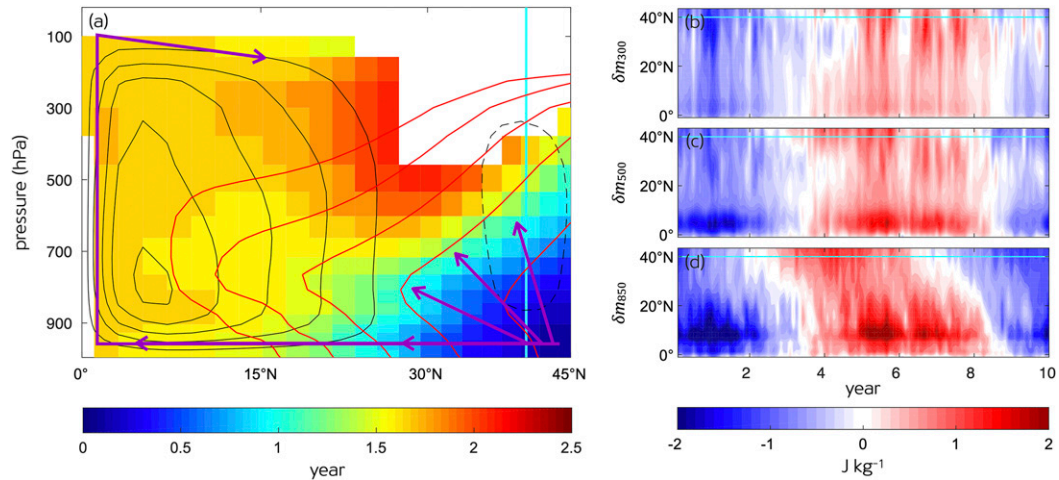
FIG. 7. (a) The lag time for which the correlation coefficient is maximized between the tropospheric zonal-mean MSE response and the Q flux forcing as a function of latitude and height (shading; unit is year) in E10. The time-mean meridional streamfunction (clockwise circulation in solid and counterclockwise circulation in dashed; interval $= 0.5 \times 10^{11}$ kg s^{-1}) and the equivalent potential temperature (red contour; interval $= 10$ K from 270 K) are from the climatology. The purple arrow illustrates the propagation pattern of zonal-mean MSE anomalies. The composite across the forcing cycle of the zonal mean MSE response at (b) 300, (c) 500, and (d) 850 hPa. The equatorial edge of the forcing region (φ_0) is indicated by a cyan line.

Since the near-surface propagation is the preferential pathway for extratropics-to-tropics teleconnection, we examine the lower atmospheric MSE propagation in more detail. Figure 9 shows the time lag of the composite zonal-mean MSE response at 900 hPa, representing the phase line of lower tropospheric MSE propagation. Based on the propagation speed, estimated by the slope of the phase line, we identify three distinct regimes

for the extratropics-to-tropics teleconnection: the midlatitude eddy regime, the subtropics transition regime, and the Hadley cell regime.

a. Midlatitude eddy regime

We decompose the atmospheric MSE flux into the mean and eddy components (see, e.g., Hill et al. 2015; Xiang et al. 2018).
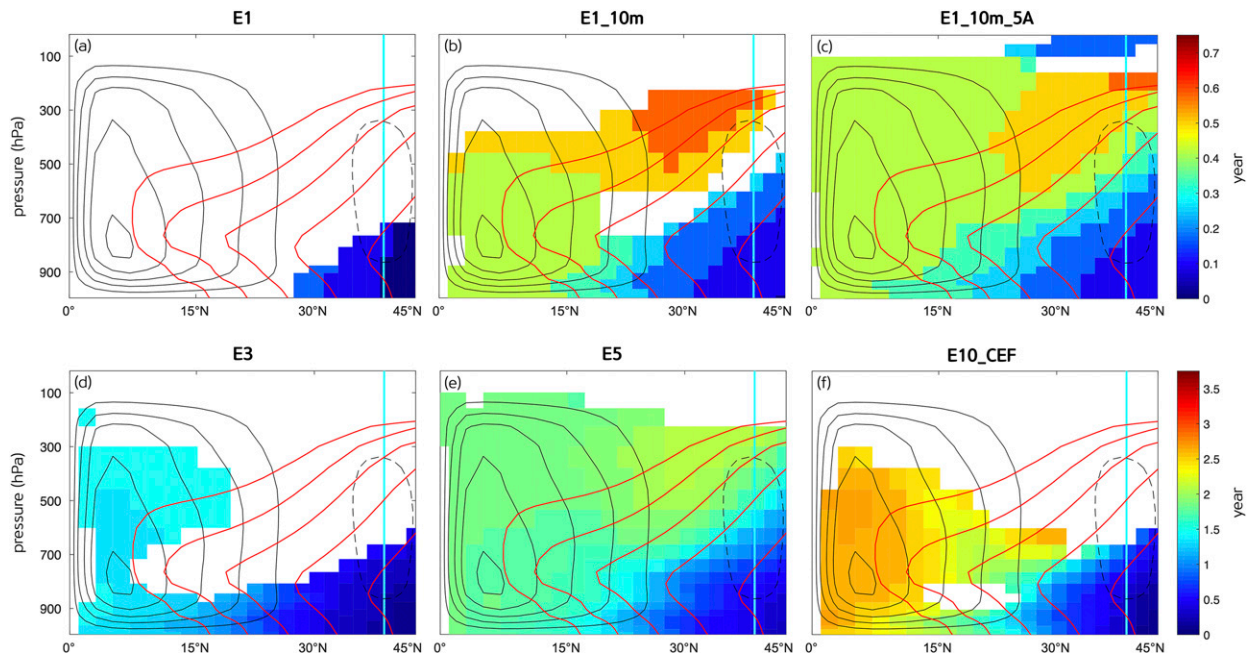

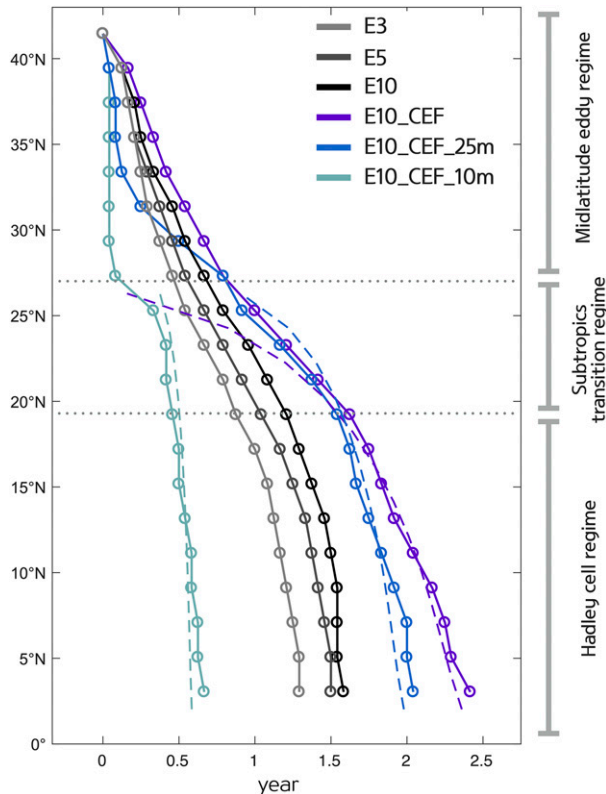FIG. 8. As in Fig. 7a, but for the (a) E1, (b) E1_10m, (c) E1_10m_5A, (d) E3, (e) E5, and (f) E10_CEF experiments.

FIG. 9. Time lag at which the lag correlation between the anomalous 900-hPa MSE at φ_0 and each latitude attains the maximum value in E3 (gray), E5 (dark gray), E10 (black), E10_CEF (purple), E10_CEF_25m (blue), and E10_CEF_10m (sky-blue). Dashed lines are the prediction by the idealized thermodynamic-advective model.

While the two components act in the opposite direction, the meridional MSE flux in the midlatitude is dominated by the eddy component in all experiments (Fig. 10a). Given the diffusive nature of eddy fluxes, we use a one-dimensional energy balance model (EBM) to predict the midlatitude response (e.g., Sellers 1969; Budyko 1969). We present the solutions to EBM governed by the following equations, in which the MSE flux at any given latitude is proportional to the surface MSE gradient (see, e.g., Hwang and Frierson 2010; Wagner and Eisenman 2015):

$$C_o \frac{\partial T_s}{\partial t} = S - L_{\mathrm{clr}} + L_{\mathrm{cld}} + Q - \frac{p_s}{g} D \nabla^2 m_s, \qquad (7)$$

where $C_o = 2 \times 10^8 \, \mathrm{J \, K^{-1} \, m^{-2}}$ is the specified heat capacity of the 50-m oceanic mixed layer, T_s is the surface temperature, S is the net incoming shortwave radiation at TOA, L_{clr} is the clear-sky outgoing longwave radiation (OLR), L_{cld} is the longwave CRE (OLR in clear sky minus OLR in all sky), Q is the imposed time-varying Q flux, and p_s is the surface pressure ($1 \times 10^5 \, \mathrm{Pa}$). The surface MSE is a function of surface temperature $m_s = c_p T_s + L_v \mathcal{H} q_s^*$ with the specific heat of dry air $c_p = 1004 \, \mathrm{J \, K^{-1} \, kg^{-1}}$, the heat of vaporization $L_v = 2.5 \times$

$10^6 \, \mathrm{J \, kg^{-1}}$, the surface relative humidity $\mathcal{H}$ (fixed as 76%), and the saturation specific humidity q_s^*, calculated using T_s in the Clausius–Clapeyron equation. The diffusion coefficient $D = 1.2 \times 10^6 \, \mathrm{m \, s^{-1}}$ is tuned to best fit the atmospheric energy flux F_A from the reference experiment. The clear-sky OLR is parameterized by the least squares regression of T_s at each latitude from the reference experiment. Because L_{clr} and m_s are a function of T_s and other terms are prescribed from the AM2.0 experiments, we can solve Eq. (7) for T_s.

Figure 11 compares the temporal evolution of the MSE flux response δF_A and the surface temperature response δT_s in all standard experiments and its prediction by the EBM. Even with the same diffusivity in the reference and perturbed experiments, both the magnitude and the phase of δF_A between 30° and 40°N are well predicted in the extratropics (Fig. 11a). The EBM also captures the sensitivity of the magnitude of extratropical SST variability to the forcing period (Fig. 11c). That is, larger SST fluctuations are predicted for lower-frequency forcing, albeit weaker in magnitude by about 20%. The overall success of EBM indicates that the eddy diffusivity is not changing but they are acting diffusively on an altered MSE gradient. The agreement between AM2.0 and EBM implies that an equatorward propagation within the extratropics is primarily accomplished by the eddy energy transport. In response to lower-frequency forcing, the eddies diffuse energy in one direction for a longer period, allowing for a larger SST response to develop (Fig. 11c).

Overlaid in Fig. 2 is the eddy heat transport response composite at its peak level of 900 hPa. Anomalous eddy heat transport is equatorward during the period of extratropical warming, while it is poleward during the period of extratropical cooling. The eddy heat transport response decreases with the forcing period, by a factor of 3 from E1 to E10, associated with smaller meridional gradients in SST anomalies. Despite the weaker eddy heat transport response for lower-frequency cases, the SST response shows a clearer equatorward propagation into the deep tropics. This is because the duration of the anomalous eddy heat transport convergence with the same sign (which corresponds to half of forcing period) increases, allowing more time for the SSTs to adjust, as suggested by the EBM. In other words, the forcing period is too short for SSTs to adjust in a high-frequency E1 case, resulting in insignificant SST responses outside the forcing region (Fig. 2a). As the SSTs require less time to adjust for a shallower mixed layer, the same high-frequency E1 forcing can induce significant SST responses outside the forcing region when $h_o \leq 40$m (Figs. 3 and 6). That is, the reason for a clearer extratropics-to-tropics teleconnection for lower-frequency extratropical forcings is because a sufficiently long time is given for SSTs outside the forcing region to respond via transient eddy fluxes. The eddy heat transport nevertheless cannot be the sole mechanism for the extratropics-to-tropics teleconnection since the eddy heat flux response is only evident in the midlatitudes and vanishes at around 20°N (Fig. 2). Consistently, the EBM fails to predict the MSE flux response in the equatorial region (Fig. 11b). The EBM-predicted δT_s also highly deviates from the actual response at low latitudes (Fig. 11c). In particular, the actual SST response is essentially muted across the equator whereas the SST response
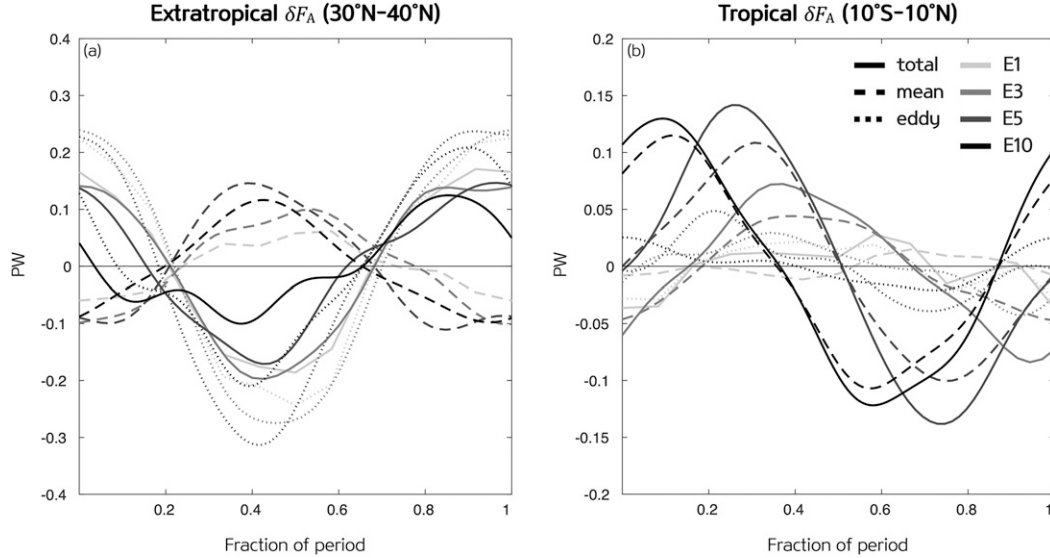
FIG. 10. Composite across the forcing cycle of the MSE flux response δF_A (solid), and its decomposition into the mean (dashed) and eddy (dotted) components averaged over (a) 30°–40°N and (b) 10°S–10°N for the E1 (light gray), E3 (gray), E5 (dark gray), and E10 (black) experiments (units are PW).

in the EBM is diffused into the Southern Hemisphere. This mismatch arises because the EBM does not account for the mean advection by the lower branch of the Hadley cell, as we show next.

b. Hadley cell regime

We now need to invoke another dynamical process responsible for the extratropics-to-tropics teleconnection at lower latitudes where eddy activity is weak. The propagation pattern of MSE anomalies in Fig. 7a suggests that a further equatorward propagation pathway resembles the climatological Hadley circulation (Fig. 7a): once the MSE response reaches the deep tropics through the lower troposphere, it quickly gets into the upper troposphere, followed by an extension into the subtropical upper troposphere (Figs. 7b–d). Furthermore, the MSE flux F_A response in the tropics is dominated by the mean component in our model (Fig. 10b). Thus, we hypothesize that the extratropics-to-tropics teleconnection is controlled by the climatological Hadley circulation that advects anomalous energy equatorward by the lower branch. Indeed, the mean MSE flux response is dominated by the thermodynamic as opposed to the dynamic component in the tropics (Fig. 12).

We adopt an idealized thermodynamical-advective model (Takahashi 2006; Takahashi et al. 2007a,b) to demonstrate the importance of mean meridional advection of MSE anomaly in the lower troposphere for the equatorward propagation of the SST response from the subtropics (i.e., the Hadley circulation terminus). The simple model represents the coupled lower atmosphere–upper ocean system. The atmospheric mixed layer (AML) is coupled to an ocean mixed layer (OML), interacting via sensible and latent heat fluxes (SHF

and LHF). The AML and OML are governed by the following equations, respectively:

$$v\frac{\partial m}{\partial y} = \text{SHF} + \text{LHF} + \mathscr{R} + \mathscr{M}, \qquad (8)$$

$$C_o\frac{\partial T_s}{\partial t} = -\text{SHF} - \text{LHF} - \mathscr{R}, \qquad (9)$$

where v is the AML meridional wind, $\mathscr{R}$ is the net radiative damping, $\mathscr{M}$ is the damping through entrainment from the free troposphere, and T_s is the OML temperature. The moist static energy in the AML is $m \equiv (L_v q + c_p T)\rho_a h_a$, with the air density $\rho_a = 1.1 \text{ kg m}^{-3}$ and the AML height $h_a = 1 \text{ km}$. We specify the OML heat capacity to be $C_o = 2 \times 10^8 \text{ J K}^{-1} \text{ m}^{-2}$ (as in our comprehensive model AM2.0). Note that we ignore the time tendency of m in Eq. (8) as the AML is assumed to be in a quasi-equilibrium state associated with a small heat capacity. Using bulk formulas and linearizing the equations with respect to the saturation specific humidity about a reference temperature, the anomalous SHF and LHF in response to Q flux can be expressed as

$$\delta\text{SHF} = \rho_a \widetilde{C_D} w_{10} c_p(\delta T_s - \delta T) \quad \text{and}$$

$$\delta\text{LHF} = \rho_a \widetilde{C_D} w_{10} L_v\left(\frac{\partial q_s}{\partial T}\delta T_s - \delta q\right), \qquad (10)$$

with δ denoting anomalous fields in response to the Q flux forcing, $\widetilde{C_D}$ the drag coefficient, and w_{10} the wind speed at the 10-m reference height. Changes in wind speed are ignored. Then, we express the sum of anomalous turbulent fluxes in terms of the moist static energy anomaly:

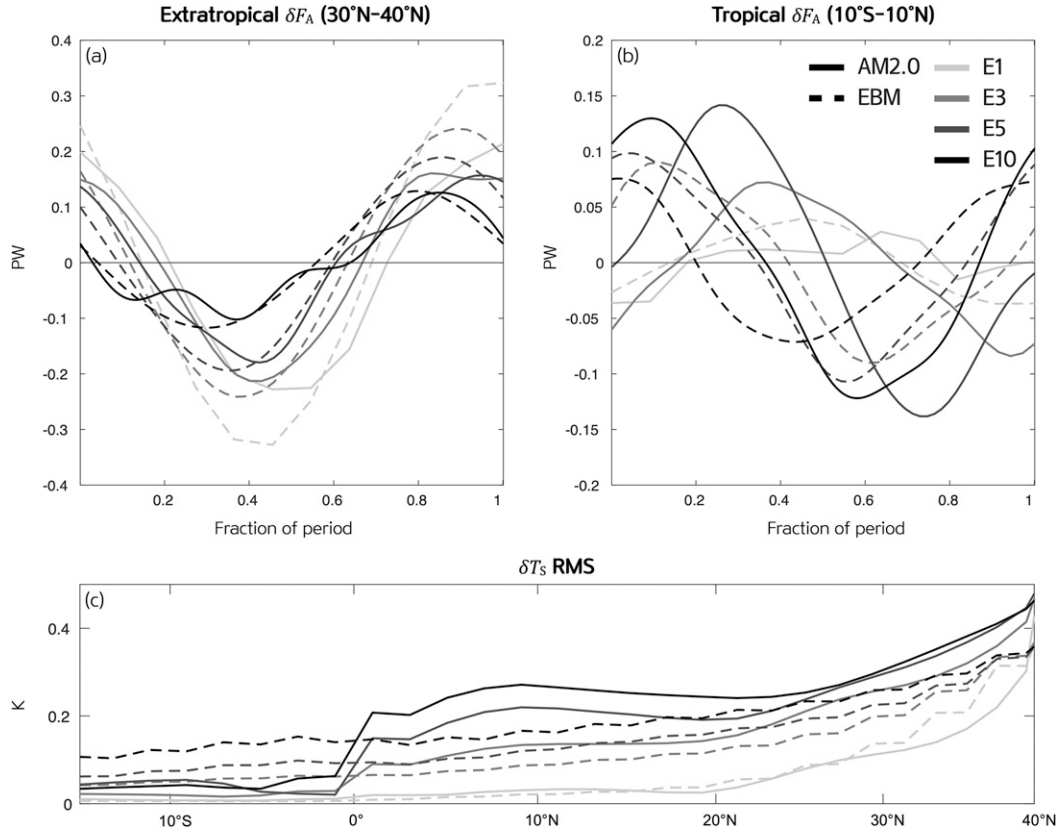$$\delta\text{SHF} + \delta\text{LHF} = C_D w_{10}(\delta m_o - \delta m), \qquad (11)$$

FIG. 11. Composite across the forcing cycle of the MSE flux response δF_A (PW) averaged over (a) 30°–40°N and (b) 10°S–10°N, and (c) the latitudinal distribution of root-mean-square of δT_S composite (K) for the E1 (light gray), E3 (gray), E5 (dark gray), and E10 (black) experiments in the AM2.0 (solid) and EBM (dashed).

where $C_D = \widetilde{C_D}/h_a$ and the equivalent heat content in the OML $\delta m_o \equiv \gamma \delta T_s$ with $\gamma \equiv [L_v(\partial q_s/\partial T) + c_p]\rho_a h_a$.

Parameterizing both the radiative and entrainment damping as Newtonian cooling, the equations for the moist static energy anomaly resulting from the prescribed extratropical forcing (Q flux) can be written as follows:

$$0 = C_D w_{10}(\delta m_o - \delta m) - (\alpha + \beta)\delta m - v\frac{\partial \delta m}{\partial y}, \quad (12)$$

$$\frac{\partial \delta m_o}{\partial t} = \frac{-\gamma C_D w_{10}}{C_o}(\delta m_o - \delta m) - \frac{\gamma \alpha}{C_o}\delta m, \quad (13)$$

where α and β are the radiative and entrainment damping rates, respectively. Because the Q flux forcing is a sinusoidal function, we seek solutions of the wavelike form:

$$\delta m = A\exp[i(ly - \omega t)] \text{ and } \delta m_o = O\exp[i(ly - \omega t)]. \quad (14)$$

Substituting Eq. (14) into the perturbation Eqs. (12) and (13) offers a dispersion relationship under the assumption of negligible radiative and entrainment damping rates (i.e., $\alpha, \beta \approx 0$):

$$\omega = \frac{\gamma C_D w_{10}}{C_o}\frac{C_D w_{10}vl - iv^2l^2}{(C_D w_{10})^2 + v^2l^2}. \quad (15)$$

One can now solve for the phase speed for large-scale waves ($l \ll 1$) as shown:

$$c = \frac{\omega}{l} = \frac{\gamma v}{C_o} = \left(\frac{L_v}{c_p}\frac{\partial q_s}{\partial T} + 1\right)\frac{C_a}{C_o}v, \quad (16)$$

where $C_a = c_p\rho_a h_a$ is the AML heat capacity. Equation (16) indicates that the phase speed c of anomalous MSE advection only depends on the background climatology. For example, a faster propagation is expected for a shallower ocean mixed layer (i.e., smaller C_o), a deeper atmospheric mixed layer (i.e., larger C_a), stronger mean meridional circulation (i.e., larger v), and/or a warmer background climate (i.e., larger $\partial q_s/\partial T$). In other words, the propagation speed is independent of forcing characteristics, and consistently the E3, E5, and E10 experiments exhibit a similar phase speed on the equatorward side of the midlatitude eddy regime (cf. the slope of achromatic solid lines equatorward of 20°N in Fig. 9).

The CRE-locked model is expected to best match the thermodynamical-advective model for which the radiative damping is neglected. Thus, we use the theoretical model to predict the propagation phase line for E10_CEF. As the CRE is locked, the tropical response time scale τ_{eq} is delayed by 10.4 months for the 50-m mixed layer simulation: $\tau_{eq} = 1.6$ yr in
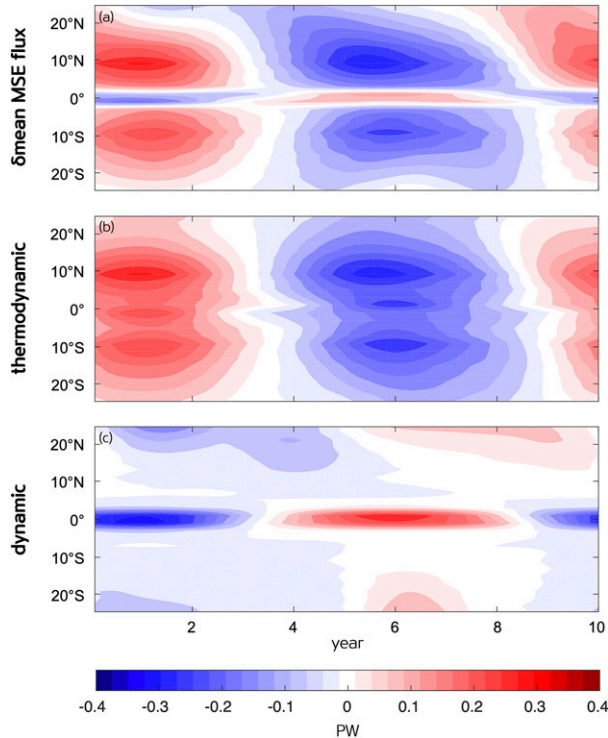
FIG. 12. Composite across the forcing cycle of the (a) mean MSE flux response $\delta F_m = \delta\langle\overline{m}\,\overline{v}\rangle = \delta(\psi_{max}H)$ and the (b) thermodynamic $\psi_{max}\delta H$ and (c) dynamic $H\delta\psi_{max}$ components between 25°S and 25°N in E10 (units are PW), where ψ_{max} is the maximum Hadley cell mass flux and H is gross moist stability (Feldl and Bordoni 2016).

E10 and $\tau_{eq} = 2.4$ yr in E10_CEF (Fig. 9). We investigate how the CRE impacts the propagation speed and pattern in section 5. By taking $(1/q_s)(\partial q_s/\partial T) \approx 7\%\,\mathrm{K}^{-1}$ and substituting meridional wind and specific humidity averaged between 1000 and 850 hPa from E10_CEF into Eq. (16), we see that our theoretical model closely reproduces the phase line in E10_CEF (contrast purple solid and dashed lines in Fig. 9). We repeat the CRE-locked experiments with mixed layer depths of 25 m (E10_CEF_25m; blue) and 10 m (E10_CEF_10m; sky-blue). The shallower the mixed layer, the faster the equatorward propagation, as discussed in section 3. Our theoretical model quantitatively captures the sensitivity to the mixed layer depth (cf. solid and dashed in Fig. 9). The E10_CEF experiment shows the propagation speed of 1.51° month^{-1} between 20°N and the equator (corresponding to the phase lag of 13.2 months), which is accelerated to 2.27° month^{-1} and 6.06° month^{-1} (corresponding to the phase lag of 8.81 months and 3.30 months) as the mixed layer depth is reduced by a factor of 2 and 5 in E10_CEF_25m and E10_CEF_10m, respectively. In sum, our thermodynamical-advective model (with no radiative feedbacks) properly predicts the propagation speed and time scale within the Hadley cell regime for CRE-locked experiments and provides an explanation for the insensitivity of the propagation speed to the forcing time scale. The results underpin our hypothesis that nondispersive moist static energy advection through the Hadley circulation return flow is the

essential mechanism for the equatorward propagation of the lower tropospheric temperature anomalies from the subtropics onward, which we refer to as the Hadley cell regime.

c. Subtropics transition regime

Between the Hadley cell and midlatitude eddy regimes exhibits a less steep phase line (Fig. 9), indicative of a damped propagation speed. This is because of the weakened eddy activities away from the extratropics and the weak mean circulation near the Hadley circulation terminus. That is, the propagation mechanism transitions from eddy-dominated to mean circulation-dominated in the subtropics. The slow subtropical transition regime could act as a rate-determining step for a sufficiently shallow mixed layer simulation where the SSTs rapidly adjust. Consistently, the subtropical transition is particularly evident in the 10-m mixed layer simulation (E10_CEF_10m).

As the SSTs in the subtropical transition regime respond to extratropical forcing, a further equatorward propagation will be taken over by the climatological Hadley cell. This implies that the ability of extratropical variability in inducing the ITCZ shift is determined by whether the SST anomalies reach the Hadley circulation terminus or not. Thus, for a cyclic extratropical forcing to shift the ITCZ, the forcing period T needs to be greater than the lag time of SST anomalies at the Hadley circulation terminus. We estimate the critical forcing period T_{crit} at which the extratropical forcing can excite the ITCZ shift as $2 \times \tau_{HC}$, where τ_{HC} indicates the lag time of maximum correlation coefficient between the SST anomaly at the Q flux edge (40°N) and at the Hadley circulation terminus (26°N in our model); τ_{HC} as a function of the mixed layer depth h_o is shown in Fig. 3. The extratropics-to-equator teleconnection emerges only for extratropical forcing with a period larger than T_{crit}, which increases with h_o. It is because $\tau_{HC} = 2.37$ months for $h_o = 10\,\mathrm{m}$ that the extratropical forcing with $T = 1$ year induces a clear teleconnection regardless of the forcing amplitude, whereas the tropical circulation and ITCZ position are hardly perturbed when $T = 1$ month (Figs. 3 and 6d). Similarly, the extratropical forcing with a 1-yr period is able to perturb the tropics for $h_o \le 40\,\mathrm{m}$ ($\tau_{HC} \le 5.50$ months) while the same forcing does not induce any tropical response when $h_o = 50\,\mathrm{m}$ ($\tau_{HC} = 8.50$ months).

5. Effect of radiative feedbacks on the extratropics-to-tropics teleconnection

Radiative feedbacks are known to modulate the equilibrium tropical response forced from the extratropics (e.g., Kang et al. 2008; Zhang et al. 2010; Seo et al. 2014; Shaw et al. 2015; White et al. 2018). However, our experiments with a periodic extratropical forcing show that the TOA radiative flux plays a limited role in modulating the degree of tropical response due to a strong cancelation between the clear-sky component (F_{CLR}; dash-dotted) and the cloud radiative effect (F_{CLD}; dashed) (Fig. 4). In this section, we examine how radiative feedbacks communicate the extratropical signal across the tropics in more detail.

The clear-sky radiation R_{CLR} poleward and equatorward of 15°N shows a distinct anomaly pattern (Fig. 13a). As the extratropics can sustain large anomalous temperatures, the SST
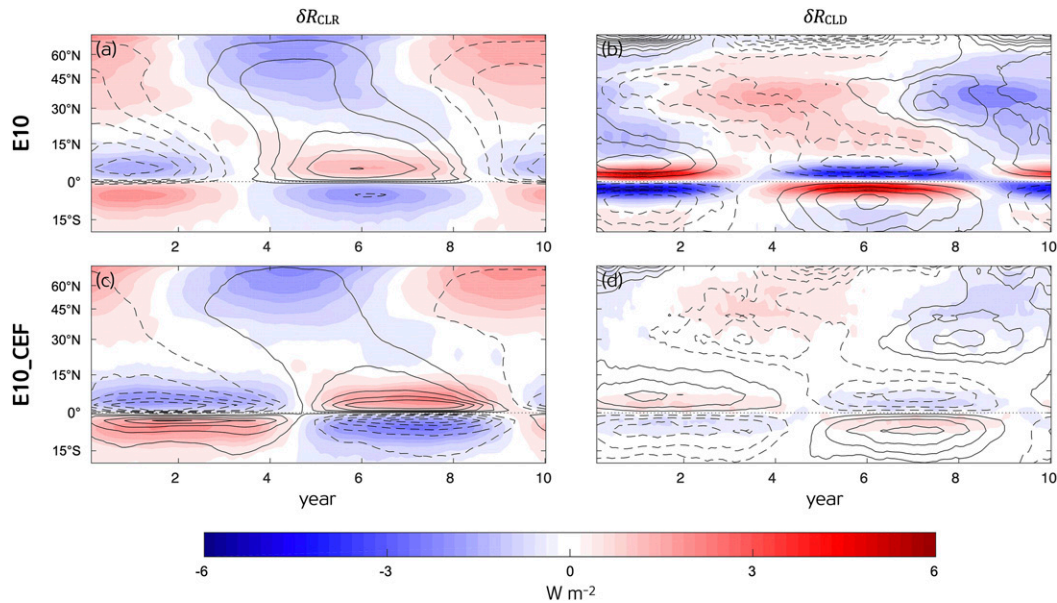
FIG. 13. Composite across the forcing cycle of zonally averaged response of (left) R_{CLR} (shading; W m^{-2}) and specific humidity at 10 m (solid/dashed contour; interval = 0.1 g kg^{-1}) and (right) R_{CLD} (shading; W m^{-2}) and LTS (solid/dashed contour; interval = 0.1 K) in the (top) E10 and (bottom) E10_CEF experiments.

increase leads to the warmer emission temperature, enhancing the clear-sky outgoing longwave radiation; the reverse applies to the SST reduction. Hence the clear-sky radiative effect poleward of 15°N serves as a negative feedback. This negative Planck feedback is weaker in the deep tropics where the temperature response is highly muted due to the weak temperature gradient criterion (Sobel et al. 2001). Instead, the deep tropical R_{CLR} response is determined by changes in water vapor (contour in Fig. 13a): thus, the clear-sky outgoing longwave radiation decreases in response to warming and increases in response to cooling, serving as a positive feedback (Clark et al. 2018).

The cloud radiative effect also shows a distinct response pattern between outside and within the deep tropics (Fig. 13b). The CRE response outside the deep tropics is tightly coupled with the collocated SST anomalies, whereas the deep tropical response is a result of the ITCZ shift. When warm SST anomalies progress to the tropics, the lower tropospheric stability (LTS; contour in Fig. 13b) decreases where LTS is defined as the difference between the potential temperature θ of the lower free troposphere (700 hPa) and the surface, LTS = $\theta_{700} - \theta_{1000}$ (Klein and Hartmann 1993). A lower LTS is accompanied by a reduction of stratiform clouds, as confirmed in both observations (Klein and Hartmann 1993) and climate models (Shaw et al. 2015; Shin et al. 2017), resulting in a reduction of shortwave reflection. Hence, associated with warmer SSTs is a positive CRE response outside the deep tropics (Fig. 13b), which serves as a positive feedback on the SST response and consequently accelerating the equatorward propagation of SST anomalies. In contrast, the CRE response within the deep tropics acts as a negative feedback on the ITCZ response. As the ITCZ shifts toward the warmer hemisphere, both low and high cloud amount increases on the warmer side of the

equator. Increased low cloud cover has a net cooling effect by reflecting more incoming shortwave radiation, whereas increased high cloud fraction has a net warming effect by reducing the outgoing longwave radiation. In our model, the CRE response in the deep tropics is dominated by the shortwave component over the longwave component (Kang et al. 2014), so that the deep tropical CRE acts as a negative feedback on the ITCZ shift. The analysis of the temporal evolution of the CRE response in E10 suggests that the CRE accelerates the equatorward progression of an extratropical signal while dampening the ITCZ response.

The role of CRE in influencing the transient tropical response is examined via a cloud locked E10_CEF experiment. The CRE response in E10_CEF does not completely vanish (Figs. 13d and 14b) because of "cloud masking" effects (Zhang et al. 1994; Soden et al. 2004) but it is substantially damped, allowing us to cleanly examine how the CRE modulates the extratropics-to-tropics teleconnection. Comparison between the standard E10 and cloud locked E10_CEF experiments (Figs. 2 and 4 vs Fig. 14) indicates that the CRE suppression decelerates the equatorward propagation of SST anomalies, delaying the ITCZ response time scale τ_{eq} by 10.4 months, while doubling the ITCZ shift extent. In other words, the interactive CRE accelerates the communication of extratropical SST anomalies to the tropics and dampens the meridional ITCZ displacement in our model.

6. Summary and conclusions

In this study, we examined the temporal evolution of the tropical precipitation response to periodic extratropical thermal perturbations in an aquaplanet GCM coupled to a slab
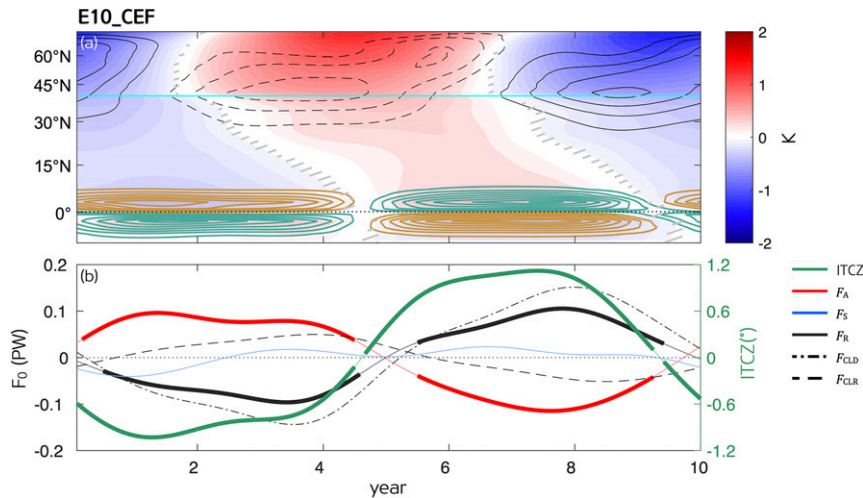
FIG. 14. (a) As in Fig. 2 and (b) as in Fig. 4, but for the E10_CEF experiment.

ocean in the absence of seasonal cycle and dynamic ocean effects. Despite broadly similar extratropical SST anomalies (by design), we find that the ITCZ response is profoundly sensitive to the time scale of extratropical forcing. In our model setting with a 50-m mixed layer, the extratropical forcing with a 3-yr and longer period induces an ITCZ response with a clear quasi-sinusoidal temporal evolution, while the ITCZ is resilient to a 1-yr period extratropical forcing. Our experiments reveal a previously unrecognized sensitivity of tropical climate response to the frequency of extratropical thermal forcing. This suggests that the ability of extratropical forcing variabilities in modulating the tropical precipitation distribution would depend on the forcing time scale. For instance, Arctic sea ice cover changes are clearly shown to shift the ITCZ in the equilibrium (Chiang and Bitz 2005; Deser et al. 2015). However, the amplified seasonality of Arctic sea ice under global warming (Haine and Martin 2017) would likely have no impact on the tropical precipitation, given that the mixed layer depth is 70 m in the northern extratropics (e.g., de Boyer Montégut et al. 2004). By contrast, a multidecadal AMOC variability should effectively induce a corresponding meridional ITCZ variability (e.g., Delworth et al. 2017). Our results highlight the important role of decadal-and-longer extratropical climate variability in shaping the tropical climate.

Our experiment configuration with a cyclic perturbation allows us to objectively identify the sequence of the atmospheric pathway. The phase lag between the periodic extratropical forcing and moist static energy indicates that the equatorward propagation occurs preferentially through the lower troposphere and undergoes three distinct regimes. In the first midlatitude regime, transient eddies play a dominant role in transporting heat equatorward until the eddy activity diminishes, as confirmed by a diffusive one-dimensional energy balance model. The critical time needed for SSTs to adjust to the eddy heat transport response creates the sensitivity of tropical precipitation response to the time scale of extratropical forcing. A high-frequency extratropical forcing grants insufficient time for SSTs to adjust away from the forcing region, limiting the

equatorward propagation of SST anomalies, and hence the ITCZ location is unperturbed. By contrast, a low-frequency extratropical forcing allows the SST anomalies to extend into the tropics, which then perturbs the tropical precipitation. As the SSTs require more time to adjust for a deeper mixed layer, the critical period at which extratropical forcing can excite an equatorward teleconnection scales with the mixed layer depth (Fig. 3). The central role of SST changes in the extratropics-to-tropics teleconnection is consistent with recent studies that show extratropical thermal perturbations can cause a meridional ITCZ shift only after the development of anomalous SSTs in the tropics (Voigt et al. 2017; Hwang et al. 2021).

In the second subtropical regime, a transition takes place from the eddy-driven to mean circulation-dominated regime. The third tropical regime is where the Hadley cell return flow advects the anomalous heat from the subtropics to the deep tropics. We devise a simple thermodynamical-advective model to demonstrate the essential role of lower tropospheric moist static energy advection in the Hadley cell regime. Neglecting any radiative feedbacks, the theoretical model nicely predicts the propagation speed in the tropics for the CRE-locked GCM experiments with a varying mixed layer depth. We emphasize that our Hadley cell advection mechanism differs from the wind–evaporation–sea surface temperature (WES) feedback (Xie and Philander 1994), which is often claimed to be an essential mechanism for the equatorward propagation of subtropical signals (Chiang and Bitz 2005). We do not expect the WES feedback to be essential because our theoretical model suggests that the propagation speed depends on the reference climate state, such as the depth and temperature of the ocean mixed layer, which is not related to the WES feedback in any direct manner. This is confirmed by the E10 experiment with a suppressed WES feedback (labeled E10_WEF), which ignores wind speed variations in the bulk aerodynamic formulation of surface turbulent fluxes (Mahajan et al. 2011; Kang and Held 2012; Kang et al. 2014). If the WES feedback were to be a key propagation mechanism, the WES feedback suppression would increase the time lag and/or reduce the amplitude of the
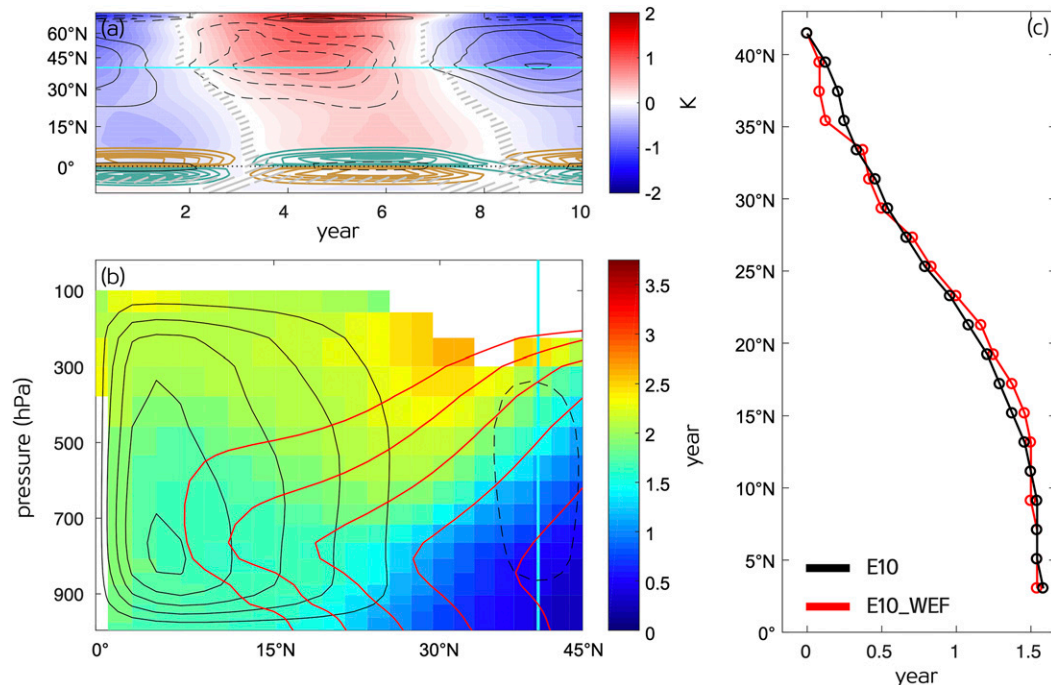
FIG. 15. (a) As in Fig. 2b, (b) as in Fig. 7a, and (c) as in Fig. 9, but for the E10_WEF experiment.

tropical response. However, the transient behavior of climate response to the periodic extratropical forcing depends little on the WES feedback (Fig. 15), suggesting that the WES feedback is not essential in the equatorward propagation of extratropical signals.

We also show that the transient response to extratropical climate variability depends on cloud radiative responses. The cloud radiative effects are known to affect the equilibrium tropical response to extratropical forcing (Kang et al. 2008; Zhang et al. 2010), and here we show that the transient behavior is also modulated by the cloud response. The cloud radiative response outside the deep tropics serves as a positive feedback, thereby accelerating the equatorward propagation of extratropical signal. By contrast, the cloud radiative effect in the deep tropics serves as a negative feedback, offsetting the tropical response. As a result, the locked cloud experiment exhibits a slower propagation of extratropical signal into the tropics and a more amplified ITCZ shift response compared to the interactive cloud experiment. However, the negative CRE in the tropics is model-dependent, as pointed out in Kang et al. (2014). This suggests that uncertainties in cloud modeling can create uncertainties in transient regional responses to climatic perturbations. For example, large uncertainties in cloud radiative effects may give rise to an uncertainty in how extratropical climate variability, such as the Atlantic multidecadal variability (AMV) and the Pacific decadal oscillation (PDO), translates into the tropics. This dependency on the cloud response suggests that our results should be tested in other GCMs.

Recent studies point to an important role of dynamic ocean in the quasi-equilibrium tropical response to extratropical radiative forcing. Dynamic ocean adjustments associated with Pacific subtropical cells and AMOC dampen the meridional ITCZ shift response to extratropical thermal forcing (Green and Marshall 2017; Yu and Pritchard 2019) and global response to Arctic sea ice loss (Deser et al. 2015). A more complete picture of extratropics-to-tropics teleconnection should be explored in a full hierarchy of coupled atmosphere–ocean–land models, but we believe the key propagation mechanism will operate through the surface, as revealed by our aquaplanet mixed layer ocean experiments.

REFERENCES

Alexander, M. A., I. Bladé, M. Newman, J. R. Lanzante, N.-C. Lau, and J. D. Scott, 2002: The atmospheric bridge: The influence of ENSO teleconnections on air–sea interaction over the global oceans. *J. Climate*, **15**, 2205–2231, https://doi.org/10.1175/1520-0442(2002)015<2205:TABTIO>2.0.CO;2.

Anderson, J. L., and Coauthors, 2004: The new GFDL global atmosphere and land model AM2–LM2: Evaluation with prescribed SST simulations. *J. Climate*, **17**, 4641–4673, https://doi.org/10.1175/JCLI-3223.1.

Biasutti, M., and A. Voigt, 2020: Seasonal and CO_2-induced shifts of the ITCZ: Testing energetic controls in idealized simulations with comprehensive models. *J. Climate*, **33**, 2853–2870, https://doi.org/10.1175/JCLI-D-19-0602.1.

Bischoff, T., and T. Schneider, 2014: Energetic constraints on the position of the intertropical convergence zone. *J. Climate*, **27**, 4937–4951, https://doi.org/10.1175/JCLI-D-13-00650.1.

——, ——, and A. N. Meckler, 2017: A conceptual model for the response of tropical rainfall to orbital variations. *J. Climate*, **30**, 8375–8391, https://doi.org/10.1175/JCLI-D-16-0691.1.

Bjerknes, J., 1969: Atmospheric teleconnections from the equatorial Pacific. *Mon. Wea. Rev.*, **97**, 163–172, https://doi.org/10.1175/1520-0493(1969)097<0163:ATFTEP>2.3.CO;2.

Broccoli, A. J., K. A. Dahl, and R. J. Stouffer, 2006: Response of the ITCZ to Northern Hemisphere cooling. *Geophys. Res. Lett.*, **33**, L01702, https://doi.org/10.1029/2005GL024546.

Bronselaer, B., M. Winton, S. M. Griffies, W. J. Hurlin, K. B. Rodgers, O. V. Sergienko, R. J. Stouffer, and J. L. Russell, 2018:Change in future climate due to Antarctic meltwater. *Nature*, **564**, 53–58, https://doi.org/10.1038/s41586-018-0712-z.

Budyko, M. I., 1969: The effect of solar radiation variations on the climate of the Earth. *Tellus*, **21**, 611–619, https://doi.org/10.1111/j.2153-3490.1969.tb00466.x.

Cabré, A., I. Marinov, and A. Gnanadesikan, 2017: Global atmospheric teleconnections and multidecadal climate oscillations driven by Southern Ocean convection. *J. Climate*, **30**, 8107–8126, https://doi.org/10.1175/JCLI-D-16-0741.1.

Chiang, J. C. H., and C. M. Bitz, 2005: Influence of high latitude ice cover on the marine Intertropical Convergence Zone. *Climate Dyn.*, **25**, 477–496, https://doi.org/10.1007/s00382-005-0040-5.

Clark, S. K., Y. Ming, I. M. Held, and P. J. Phillipps, 2018: The role of the water vapor feedback in the ITCZ response to hemispherically asymmetric forcings. *J. Climate*, **31**, 3659–3678, https://doi.org/10.1175/JCLI-D-17-0723.1.

Cvijanovic, I., and J. C. H. Chiang, 2013: Global energy budget changes to high latitude North Atlantic cooling and the tropical ITCZ response. *Climate Dyn.*, **40**, 1435–1452, https://doi.org/10.1007/s00382-012-1482-1.

de Boyer Montégut, C., G. Madec, A. S. Fischer, A. Lazar, and D. Iudicone, 2004: Mixed layer depth over the global ocean: An examination of profile data and a profile-based climatology. *J. Geophys. Res. Oceans*, **109**, C12003, https://doi.org/10.1029/2004JC002378.

Delworth, T. L., F. Zeng, L. Zhang, R. Zhang, G. A. Vecchi, and X. Yang, 2017: The central role of ocean dynamics in connecting the North Atlantic Oscillation to the extratropical component of the Atlantic multidecadal oscillation. *J. Climate*, **30**, 3789–3805, https://doi.org/10.1175/JCLI-D-16-0358.1.

Deser, C., R. A. Tomas, and L. Sun, 2015: The role of ocean–atmosphere coupling in the zonal-mean atmospheric response to Arctic sea ice loss. *J. Climate*, **28**, 2168–2186, https://doi.org/10.1175/JCLI-D-14-00325.1.

Donohoe, A., and A. Voigt, 2017: Why future shifts in tropical precipitation will likely be small: The location of the tropical rain belt and the hemispheric contrast of energy input to the atmosphere. *Climate Extremes Patterns Mech.*, **226**, 115–137, https://doi.org/10.1002/9781119068020.ch8.

——, J. Marshall, D. Ferreira, and D. McGee, 2013: The relationship between ITCZ location and cross-equatorial atmospheric heat transport: From the seasonal cycle to the Last Glacial Maximum. *J. Climate*, **26**, 3597–3618, https://doi.org/10.1175/JCLI-D-12-00467.1.

——, ——, ——, K. Armour, and D. McGee, 2014: The interannual variability of tropical precipitation and interhemispheric energy transport. *J. Climate*, **27**, 3377–3392, https://doi.org/10.1175/JCLI-D-13-00499.1.

Feldl, N., and S. Bordoni, 2016: Characterizing the Hadley circulation response through regional climate feedbacks. *J. Climate*, **29**, 613–622, https://doi.org/10.1175/JCLI-D-15-0424.1.

Frierson, D. M. W., and Y.-T. Hwang, 2012: Extratropical influence on ITCZ shifts in slab ocean simulations of global warming. *J. Climate*, **25**, 720–733, https://doi.org/10.1175/JCLI-D-11-00116.1.

——, and Coauthors, 2013: Contribution of ocean overturning circulation to tropical rainfall peak in the Northern Hemisphere. *Nat. Geosci.*, **6**, 940–944, https://doi.org/10.1038/ngeo1987.

Green, B., and J. Marshall, 2017: Coupling of trade winds with ocean circulation damps ITCZ shifts. *J. Climate*, **30**, 4395–4411, https://doi.org/10.1175/JCLI-D-16-0818.1.

——, ——, and A. Donohoe, 2017: Twentieth century correlations between extratropical SST variability and ITCZ shifts. *Geophys. Res. Lett.*, **44**, 9039–9047, https://doi.org/10.1002/2017GL075044.

——, ——, and J.-M. Campin, 2019: The 'sticky' ITCZ: Ocean-moderated ITCZ shifts. *Climate Dyn.*, **53** (1–2), 1–19, https://doi.org/10.1007/s00382-019-04623-5.

Haine, T. W. N., and T. Martin, 2017: The Arctic-Subarctic sea ice system is entering a seasonal regime: Implications for future Arctic amplification. *Sci. Rep.*, **7**, 4618, https://doi.org/10.1038/s41598-017-04573-0.

Hawcroft, M., J. M. Haywood, M. Collins, A. Jones, A. C. Jones, and G. Stephens, 2017: Southern Ocean albedo, inter-hemispheric energy transports and the double ITCZ: Global impacts of biases in a coupled model. *Climate Dyn.*, **48**, 2279–2295, https://doi.org/10.1007/s00382-016-3205-5.

Hill, S. A., 2019: Theories for past and future monsoon rainfall changes. *Curr. Climate Change Rep.*, **5**, 160–171, https://doi.org/10.1007/s40641-019-00137-8.

——, Y. Ming, and I. M. Held, 2015: Mechanisms of forced tropical meridional energy flux change. *J. Climate*, **28**, 1725–1742, https://doi.org/10.1175/JCLI-D-14-00165.1.

Horel, J. D., and J. M. Wallace, 1981: Planetary-scale atmospheric phenomena associated with the Southern Oscillation. *Mon. Wea. Rev.*, **109**, 813–829, https://doi.org/10.1175/1520-0493(1981)109<0813:PSAPAW>2.0.CO;2.

Hoskins, B. J., and D. J. Karoly, 1981: The steady linear response of a spherical atmosphere to thermal and orographic forcing. *J. Atmos. Sci.*, **38**, 1179–1196, https://doi.org/10.1175/1520-0469(1981)038<1179:TSLROA>2.0.CO;2.

——, and T. Ambrizzi, 1993: Rossby wave propagation on a realistic longitudinally varying flow. *J. Atmos. Sci.*, **50**, 1661–1671, https://doi.org/10.1175/1520-0469(1993)050<1661:RWPOAR>2.0.CO;2.

Hwang, Y.-T., and D. M. W. Frierson, 2010: Increasing atmospheric poleward energy transport with global warming. *Geophys. Res. Lett.*, **37**, L24 807, https://doi.org/10.1029/2010GL045440.

——, H.-Y. Tseng, K.-C. Li, S. M. Kang, Y.-J. Chen, and J. C. H. Chiang, 2021: Relative roles of energy and momentum fluxes in the tropical response to extratropical thermal forcing. *J. Climate*, **34**, 3771–3786, https://doi.org/10.1175/JCLI-D-20-0151.1.

Kang, S. M., 2020: Extratropical influence on the tropical rainfall distribution. *Curr. Climate Change Rep.*, **6** (2), 1–13, https://doi.org/10.1007/s40641-020-00154-y.

——, and I. M. Held, 2012: Tropical precipitation, SSTs and the surface energy budget: A zonally symmetric perspective. *Climate Dyn.*, **38**, 1917–1924, https://doi.org/10.1007/s00382-011-1048-7.

——, ——, D. M. W. Frierson, and M. Zhao, 2008: The response of the ITCZ to extratropical thermal forcing: Idealized slab-ocean experiments with a GCM. *J. Climate*, **21**, 3521–3532, https://doi.org/10.1175/2007JCLI2146.1.

——, D. M. W. Frierson, and I. M. Held, 2009: The tropical response to extratropical thermal forcing in an idealized GCM: The importance of radiative feedbacks and convective parameterization. *J. Atmos. Sci.*, **66**, 2812–2827, https://doi.org/10.1175/2009JAS2924.1.

——, I. M. Held, and S.-P. Xie, 2014: Contrasting the tropical responses to zonally asymmetric extratropical and tropical thermal forcing. *Climate Dyn.*, **42**, 2033–2043, https://doi.org/10.1007/s00382-013-1863-0.

——, B.-M. Kim, D. M. W. Frierson, S.-J. Jeong, J. Seo, and Y. Chae, 2015a: Seasonal dependence of the effect of Arctic greening on tropical precipitation. *J. Climate*, **28**, 6086–6095, https://doi.org/10.1175/JCLI-D-15-0079.1.

——, R. Seager, D. M. W. Frierson, and X. Liu, 2015b: Croll revisited: Why is the Northern Hemisphere warmer than the Southern Hemisphere? *Climate Dyn.*, **44**, 1457–1472, https://doi.org/10.1007/s00382-014-2147-z.

——, Y. Shin, and S.-P. Xie, 2018a: Extratropical forcing and tropical rainfall distribution: Energetics framework and ocean Ekman advection. *npj Climate Atmos. Sci.*, **1**, 20172, https://doi.org/10.1038/s41612-017-0004-6.

——, ——, and F. Codron, 2018b: The partitioning of poleward energy transport response between the atmosphere and Ekman flux to prescribed surface forcing in a simplified GCM. *Geosci. Lett.*, **5** (1), 22, https://doi.org/10.1186/s40562-018-0124-9.

——, and Coauthors, 2019: Extratropical-Tropical Interaction Model Intercomparison Project (ETIN-MIP): Protocol and initial results. *Bull. Amer. Meteor. Soc.*, **100**, 2589–2606, https://doi.org/10.1175/BAMS-D-18-0301.1.

——, S.-P. Xie, Y. Shin, H. Kim, Y.-T. Hwang, M. F. Stuecker, B. Xiang, and M. Hawcroft, 2020: Walker circulation response to extratropical radiative forcing. *Sci. Adv.*, **6**, eabd3021, https://doi.org/10.1126/sciadv.abd3021.

Kay, J. E., C. Wall, V. Yettella, B. Medeiros, C. Hannay, P. Caldwell, and C. Bitz, 2016: Global climate impacts of fixing the Southern Ocean shortwave radiation bias in the Community Earth System Model (CESM). *J. Climate*, **29**, 4617–4636, https://doi.org/10.1175/JCLI-D-15-0358.1.

Kim, D., S. M. Kang, Y. Shin, and N. Feldl, 2018: Sensitivity of polar amplification to varying insolation conditions. *J. Climate*, **31**, 4933–4947, https://doi.org/10.1175/JCLI-D-17-0627.1.

Klein, S. A., and D. L. Hartmann, 1993: The seasonal cycle of low stratiform clouds. *J. Climate*, **6**, 1587–1606, https://doi.org/10.1175/1520-0442(1993)006<1587:TSCOLS>2.0.CO;2.

Koutavas, A., and J. Lynch-Stieglitz, 2004: Variability of the marine ITCZ over the eastern Pacific during the past 30,000 years. *The Hadley Circulation: Present, Past and Future*, H. F. Diaz and R. S. Bradley, Eds., Springer, 347–369.

Kraus, E. B., 1977: Subtropical droughts and cross-equatorial energy transports. *Mon. Wea. Rev.*, **105**, 1009–1018, https://doi.org/10.1175/1520-0493(1977)105<1009:SDACEE>2.0.CO;2.

Lea, D. W., D. K. Pak, L. C. Peterson, and K. A. Hughen, 2003: Synchroneity of tropical and high-latitude Atlantic temperatures over the last glacial termination. *Science*, **301**, 1361–1364, https://doi.org/10.1126/science.1088470.

Li, X., D. M. Holland, E. P. Gerber, and C. Yoo, 2014: Impacts of the north and tropical Atlantic Ocean on the Antarctic Peninsula and sea ice. *Nature*, **505**, 538–542, https://doi.org/10.1038/nature12945.

Mahajan, S., R. Saravanan, and P. Chang, 2011: The role of the wind–evaporation–sea surface temperature (WES) feedback as a thermodynamic pathway for the equatorward propagation of high-latitude sea ice–induced cold anomalies. *J. Climate*, **24**, 1350–1361, https://doi.org/10.1175/2010JCLI3455.1.

Marshall, J., A. Donohoe, D. Ferreira, and D. McGee, 2014: The ocean's role in setting the mean position of the Inter-Tropical Convergence Zone. *Climate Dyn.*, **42**, 1967–1979, https://doi.org/10.1007/s00382-013-1767-z.

Moreno-Chamarro, E., J. Marshall, and T. L. Delworth, 2020: Linking ITCZ migrations to the AMOC and North Atlantic/Pacific SST decadal variability. *J. Climate*, **33**, 893–905, https://doi.org/10.1175/JCLI-D-19-0258.1.

Peterson, L. C., G. H. Haug, K. A. Hughen, and U. Röhl, 2000: Rapid changes in the hydrologic cycle of the tropical Atlantic during the last glacial. *Science*, **290**, 1947–1951, https://doi.org/10.1126/science.290.5498.1947.

Roberts, W. H. G., P. J. Valdes, and J. S. Singarayer, 2017: Can energy fluxes be used to interpret glacial/interglacial precipitation changes in the tropics? *Geophys. Res. Lett.*, **44**, 6373–6382, https://doi.org/10.1002/2017GL073103.

Sardeshmukh, P. D., and B. J. Hoskins, 1988: The generation of global rotational flow by steady idealized tropical divergence. *J. Atmos. Sci.*, **45**, 1228–1251, https://doi.org/10.1175/1520-0469(1988)045<1228:TGOGRF>2.0.CO;2.

Schneider, E. K., and I. G. Watterson, 1984: Stationary Rossby wave propagation through easterly layers. *J. Atmos. Sci.*, **41**, 2069–2083, https://doi.org/10.1175/1520-0469(1984)041<2069:SRWPTE>2.0.CO;2.

Schneider, T., 2017: Feedback of atmosphere–ocean coupling on shifts of the intertropical convergence zone. *Geophys. Res. Lett.*, **44**, 11,644–653, https://doi.org/10.1002/2017GL075817.

Sellers, W. D., 1969: A global climatic model based on the energy balance of the Earth–atmosphere system. *J. Appl. Meteor. Climatol.*, **8**, 392–400, https://doi.org/10.1175/1520-0450(1969)008<0392:AGCMBO>2.0.CO;2.

Seo, J., S. M. Kang, and D. M. W. Frierson, 2014: Sensitivity of intertropical convergence zone movement to the latitudinal position of thermal forcing. *J. Climate*, **27**, 3035–3042, https://doi.org/10.1175/JCLI-D-13-00691.1.

——, ——, and T. M. Merlis, 2017: A model intercomparison of the tropical precipitation response to a CO_2 doubling in aquaplanet simulations. *Geophys. Res. Lett.*, **44**, 993–1000, https://doi.org/10.1002/2016GL072347.

Shaw, T. A., A. Voigt, S. M. Kang, and J. Seo, 2015: Response of the intertropical convergence zone to zonally asymmetric subtropical surface forcings. *Geophys. Res. Lett.*, **42**, 9961–9969, https://doi.org/10.1002/2015GL066027.

Shin, Y., S. M. Kang, and M. Watanabe, 2017: Dependence of Arctic climate on the latitudinal position of stationary waves and to high-latitudes surface warming. *Climate Dyn.*, **49**, 3753–3763, https://doi.org/10.1007/s00382-017-3543-y.

Singh, M. S., Z. Kuang, and Y. Tian, 2017: Eddy influences on the strength of the Hadley circulation: Dynamic and thermodynamic perspectives. *J. Atmos. Sci.*, **74**, 467–486, https://doi.org/10.1175/JAS-D-16-0238.1.

Sobel, A. H., J. Nilsson, and L. M. Polvani, 2001: The weak temperature gradient approximation and balanced tropical moisture waves. *J. Atmos. Sci.*, **58**, 3650–3665, https://doi.org/10.1175/1520-0469(2001)058<3650:TWTGAA>2.0.CO;2.

Soden, B. J., A. J. Broccoli, and R. S. Hemler, 2004: On the use of cloud forcing to estimate cloud feedback. *J. Climate*, **17**,

3661–3665, https://doi.org/10.1175/1520-0442(2004)017<3661:OTUOCF>2.0.CO;2.

Stouffer, R. J., and Coauthors, 2006: Investigating the causes of the response of the thermohaline circulation to past and future climate changes. *J. Climate*, **19**, 1365–1387, https://doi.org/10.1175/JCLI3689.1.

Stuecker, M. F., and Coauthors, 2020: Strong remote control of future equatorial warming by off-equatorial forcing. *Nat. Climate Change*, **10**, 124–129, https://doi.org/10.1038/s41558-019-0667-6.

Swann, A. L. S., I. Y. Fung, and J. C. H. Chiang, 2012: Mid-latitude afforestation shifts general circulation and tropical precipitation. *Proc. Natl. Acad. Sci. USA*, **109**, 712–716, https://doi.org/10.1073/pnas.1116706108.

Takahashi, K., 2006: Processes controlling the tropical Pacific mean precipitation pattern. Ph.D. dissertation, University of Washington, 135 pp.

——, and D. S. Battisti, 2007a: Processes controlling the mean tropical Pacific precipitation pattern. Part I: The Andes and the eastern Pacific ITCZ. *J. Climate*, **20**, 3434–3451, https://doi.org/10.1175/JCLI4198.1.

——, and ——, 2007b: Processes controlling the mean tropical Pacific precipitation pattern. Part II: The SPCZ and the southeast Pacific dry zone. *J. Climate*, **20**, 5696–5706, https://doi.org/10.1175/2007JCLI1656.1.

Timmermann, A., and Coauthors, 2018: El Niño–southern oscillation complexity. *Nature*, **559**, 535–545, https://doi.org/10.1038/s41586-018-0252-6.

Trenberth, K. E., G. W. Branstator, D. Karoly, A. Kumar, N. Lau, and C. Ropelewski, 1998: Progress during TOGA in understanding and modeling global teleconnections associated with tropical sea surface temperatures. *J. Geophys. Res. Oceans*, **103**, 14 291–14 324, https://doi.org/10.1029/97JC01444.

Voigt, A., and Coauthors, 2017: Fast and slow shifts of the zonal-mean intertropical convergence zone in response to an idealized anthropogenic aerosol. *J. Adv. Model. Earth Syst.*, **9**, 870–892, https://doi.org/10.1002/2016MS000902.

Wagner, T. J. W., and I. Eisenman, 2015: How climate model complexity influences sea ice stability. *J. Climate*, **28**, 3998–4014, https://doi.org/10.1175/JCLI-D-14-00654.1.

Wallace, J. M., and D. S. Gutzler, 1981: Teleconnections in the geopotential height field during the Northern Hemisphere winter. *Mon. Wea. Rev.*, **109**, 784–812, https://doi.org/10.1175/1520-0493(1981)109<0784:TITGHF>2.0.CO;2.

Wang, X., A. S. Auler, R. L. Edwards, H. Cheng, P. S. Cristalli, P. L. Smart, D. A. Richards, and C.-C. Shen, 2004: Wet periods in northeastern Brazil over the past 210 kyr linked to distant climate anomalies. *Nature*, **432**, 740–743, https://doi.org/10.1038/nature03067.

Wang, Y.-J., H. Cheng, R. L. Edwards, Z. S. An, J. Y. Wu, C.-C. Shen, and J. A. Dorale, 2001: A high-resolution absolute-dated late Pleistocene monsoon record from Hulu Cave, China. *Science*, **294**, 2345–2348, https://doi.org/10.1126/science.1064618.

Wei, H., and S. Bordoni, 2018: Energetic constraints on the ITCZ position in idealized simulations with a seasonal cycle. *J. Adv. Model. Earth Syst.*, **10**, 1708–1725, https://doi.org/10.1029/2018MS001313.

White, R. H., A. A. McFarlane, D. M. W. Frierson, S. M. Kang, Y. Shin, and M. Friedman, 2018: Tropical precipitation and cross-equatorial heat transport in response to localized heating: Basin and hemisphere dependence. *Geophys. Res. Lett.*, **45**, 11 949–11 958, https://doi.org/10.1029/2018GL078781.

Woelfle, M. D., C. S. Bretherton, and D. M. W. Frierson, 2015: Time scales of response to antisymmetric surface fluxes in an aquaplanet GCM. *Geophys. Res. Lett.*, **42**, 2555–2562, https://doi.org/10.1002/2015GL063372.

Xiang, B., M. Zhao, Y. Ming, W. Yu, and S. M. Kang, 2018: Contrasting impacts of radiative forcing in the Southern Ocean versus southern tropics on ITCZ position and energy transport in one GFDL climate model. *J. Climate*, **31**, 5609–5628, https://doi.org/10.1175/JCLI-D-17-0566.1.

Xie, S., 2004: The shape of continents, air–sea interaction, and the rising branch of the Hadley circulation. *The Hadley Circulation: Present, Past and Future*, H. F. Diaz and R. S. Bradley, Eds., Springer, 121–152.

——, and S. G. H. Philander, 1994: A coupled ocean–atmosphere model of relevance to the ITCZ in the eastern Pacific. *Tellus*, **46A**, 340–350, https://doi.org/10.3402/tellusa.v46i4.15484.

Yoshimori, M., and A. J. Broccoli, 2008: Equilibrium response of an atmosphere–mixed layer ocean model to different radiative forcing agents: Global and zonal mean response. *J. Climate*, **21**, 4399–4423, https://doi.org/10.1175/2008JCLI2172.1.

Yu, S., and M. S. Pritchard, 2019: A strong role for the AMOC in partitioning global energy transport and shifting ITCZ position in response to latitudinally discrete solar forcing in CESM1.2. *J. Climate*, **32**, 2207–2226, https://doi.org/10.1175/JCLI-D-18-0360.1.

Zhang, M. H., J. J. Hack, J. T. Kiehl, and R. D. Cess, 1994: Diagnostic study of climate feedback processes in atmospheric general circulation models. *J. Geophys. Res.*, **99**, 5525–5537, https://doi.org/10.1029/93JD03523.

Zhang, R., and T. L. Delworth, 2005: Simulated tropical response to a substantial weakening of the Atlantic thermohaline circulation. *J. Climate*, **18**, 1853–1860, https://doi.org/10.1175/JCLI3460.1.

——, S. M. Kang, and I. M. Held, 2010: Sensitivity of climate change induced by the weakening of the Atlantic meridional overturning circulation to cloud feedback. *J. Climate*, **23**, 378–389, https://doi.org/10.1175/2009JCLI3118.1.